2011

The Emergence of Collective Phenomena in Systems with Random Interactions

Volha Abramkina

THE FLORIDA STATE UNIVERSITY

COLLEGE OF ARTS AND SCIENCES

THE EMERGENCE OF COLLECTIVE PHENOMENA IN SYSTEMS WITH RANDOM INTERACTIONS

By

VOLHA ABRAMKINA

A Thesis submitted to the
Department of Physics
in partial fulfillment of the
requirements for the degree of
Doctorate of Philosophy in Physics

Degree Awarded:
Summer Semester, 2011

The members of the committee approve the thesis of Volha Abramkina defended on May 17, 2011.

Alexander Volya
Professor Directing Thesis

Giray Ökten
University Representative

Simon Capstick
Committee Member

Grigory Rogachev
Committee Member

Per Arne Rikvold
Committee Member

Approved:

Mark Riley, Chair, Department of Physics

Joseph Travis, Dean, College of Arts and Sciences

The Graduate School has verified and approved the above-named committee members.

ACKNOWLEDGMENTS

With great pleasure I would like to acknowledge my colleagues and friends for their contribution to this work and express my sincere gratitude for their support.

First and foremost, I would like to thank my advisor, Dr. Alexander Volya. It was my privilege to conduct my research under his guidance. His extensive knowledge of physics, ability to put things in perspective, and infinite patience were critical to my success.

I would also like to acknowledge the important contribution of Dr. Vladimir Zelevinsky from Michigan State University to shaping the ideas for this work.

I would like to offer my gratitude to Dr. Simon Capstick and Dr. Jorge Pekarewicz for their kindness and for sharing their endless knowledge and enthusiasm.

I would like to thank Dr. Simon Capstick, Dr. Grigory Rogachev, Dr. Per Arne Rikvold, and Dr. Giray Ökten for serving on my dissertation committee, their close attention to this work, and helpful suggestions that improved the quality of the manuscript.

Many thanks go out to the former and current students in the nuclear theory group: Benjamin Eakins, Farrukh Fattoyev, Dr. Alvin Kiswandhi, Dr. Muslema Pervin, Dr. Tony Sumaryada, Dr. Jutri Taruna. Our discussions broadened my views of science and motivated me in my work. Being in the same boat, you were giving me comfort so much needed in the times of inevitable slumps.

I am very grateful to Dr. Vandana Tripathi and Dr. Kurtis Johnson for their professional guidance and discussions and a good laughter we shared.

Of particular note are my dearest friends and office-mates: Naureen Ahsan, David

Morris, and Anna Woodard. Thank you for being my friends, your presence and support were vital for me all these years. I hope your wisdom, kindness, and sense of humor have been transmitted to me through "some higher order mechanism."

This work was supported in part by the United States Department of Energy, grant No.DE-FG02-92ER40750. The computing resources were provided by the Florida State University shared High-Performance Computing facility.

TABLE OF CONTENTS

LIST OF TABLES

LIST OF FIGURES

ABSTRACT

Emergent phenomena are one of the most profound topics in modern science, addressing the ways that collectivities and complex patterns appear due to multiplicity of components and simple interactions. Ensembles of random Hamiltonians allow one to explore emergent phenomena in a statistical way. In this work we adopt a shell model approach with a two-body interaction Hamiltonian. The sets of the two-body interaction strengths are selected at random, resulting in the two-body random ensemble (TBRE). Symmetries such as angular momentum, isospin, and parity entangled with complex many-body dynamics result in surprising order discovered in the spectrum of low-lying excitations. The statistical patterns exhibited in the TBRE are remarkably similar to those observed in real nuclei. Signs of almost every collective feature seen in nuclei, namely, pairing superconductivity, deformation, and vibration, have been observed in random ensembles [3, 4, 5, 6]. In what follows a systematic investigation of nuclear shape collectivities in random ensembles is conducted. The development of the mean field, its geometry, multipole collectivities and their dependence on the underlying two-body interaction are explored. Apart from the role of static symmetries such as SU(2) angular momentum and isospin groups, the emergence of dynamical symmetries including the seniority SU(2), rotational symmetry, as well as the Elliot SU(3) is shown to be an important precursor for the existence of geometric collectivities.

CHAPTER 1

INTRODUCTION

Models are at the core of our understanding of nuclear structure. One of the first proposed models of a nucleus, the liquid drop model, is built on the assumption of strong interactions among nucleons; a low compressibility and a sharply defined surface in nuclei resemble properties of liquids. With some work done previously by Gamow, Heisenberg, and Weizsacker, the main contribution to the development of the model was made by Niels Bohr in 1936. The model predicts the main features of the nuclear binding energy systematics, and it has also been successful at describing nuclear fission.

What the liquid drop model cannot explain is the shell structure observed in nuclei: some "magic" nuclei are noticeably more stable than their neighbors. The existence of the magic numbers, numbers of neutrons and protons comprising these specially stable nuclei, gave rise to the idea of the nuclear shell model. It appears that the nuclear shell model and the liquid drop model are based on mutually exclusive assumptions. In the non-interacting shell model the nucleons are moving independently in the common mean field. The nuclear magic numbers were not explained until the spin-orbit splitting was added to the mean field potential. Development of the nuclear shell model earned Maria Goeppert-Mayer and J. Hans D. Jensen the Nobel Prize in Physics 1963.

The success of the shell model was overshadowed by the discoveries of collective,

which seems to be incompatible with an independent particle picture, behavior in nuclei, such as large electromagnetic moments and transition rates and the discovery of the rotational bands. Deformations and rotational motion were explained by the collective model of A. Bohr and B. Mottelson [2] which is based on the liquid drop model. Later the single-particle and collective approaches have been unified and three physicists, A. Bohr, B. Mottelson, and J. Rainwater, were awarded with the 1975 Nobel Prize "for the discovery of the connection between collective motion and particle motion in atomic nuclei".

With computational advances it became possible to perform shell-model calculations with many valence nucleons, and the link between microscopic (single-particle) and macroscopic (collective) descriptions has been clarified further. An important milestone was set by the Elliot SU(3) model [7]. The model provides a classification of the shell model many-body configurations according to the SU(3) symmetry group and gives an insight into into how mixing of the spherical configurations can lead to deformed nuclear shapes. The SU(3) symmetry is violated by such important components of nuclear interaction as spin-orbit interaction and pairing. One of the objectives of the present work is a study of deformations and rotations in the shell model in cases when the SU(3) symmetry is broken. Another, more general objective is an investigation of the formation of collective modes in the shell model. This can be done by means of the two-body random ensemble (TBRE).

The idea of employing systems described by an ensemble of Hamiltonians with random matrix elements is the foundation of random matrix theory (RMT). Random matrix theory offers a statistical approach to strongly interacting quantum systems. Motivated by Bohr's idea of a compound nucleus, Wigner introduced random matrix theory [8]. A model of a compound nucleus [9] was proposed in order to explain numerous narrow resonances in slow neutron scattering, which cannot be described in the independent particle picture. The idea is that the target nucleus absorbs the pro-

jectile particle, forming a new excited long-lived compound nucleus with the energy of the projectile distributed among all nucleons. Such scattering can be visualized as a billiard table densely filled with balls (protons and neutrons) that undergo multiple collisions. The RMT approach allows one to look for the manifestation of generic spectral features emerging in complex systems, without a reference to specifics of the Hamiltonian. RMT is employed in many branches of physics, including nuclear structure and reactions, condensed matter, and quantum chaos.

The canonical RMT ensemble, a Gaussian orthogonal ensemble (GOE), is applicable to systems invariant under time reversal. GOE matrices defined in a finite Hilbert space are characterized by the following four properties: (i) hermiticity, (ii) time-reversal invariance, (iii) invariance of the probability distribution of the matrices under an arbitrary orthogonal transformation of basis, and (iv) independence of the matrix elements. As a result of these requirements, the matrix elements should be chosen from a Gaussian distribution centered around zero with the variance of the off-diagonal elements doubled compared to the diagonal ones. One can refer to Bohr and Mottelson [2] for an illustrative example with derivations for a two-level system and to Mehta [10] for a detailed description of random-matrix approach and methods.

The GOE predicts fluctuation properties of eigenstates and eigenvalues for the many-body chaos appearing due to the complexity of many-body dynamics, and one-body chaos which is due to the boundary conditions. The advantage of GOE is its analytical tractability. In the GOE each state is connected with the rest of the states with matrix elements of the same order of magnitude. The shortcoming of the ensemble is its lack of a connection with the actual many-body dynamics. There is no preferred basis in the GOE, as it is the case in the mean-field models. This also implies a high rank of forces, which is unrealistic in nuclear physics: in the shell model it is sufficient to consider two-body forces. These drawbacks result in unrealistic predictions for average spectral properties such as the energy-level density, which is

semicircular in the GOE and Gaussian in the shell model. The first step in reconciling the underlying many-body physics and random ensembles was an implementation of embedded ensembles with a lower (down to the second) rank of forces [11]. With the transition from many-body to two-body forces, the energy density distribution undergoes the semicircle-to-Gaussian transition. The incorporation of the angular momentum conservation led to the two-body random ensemble (TBRE), which mimics the nuclear shell model [12, 13].

In full analogy to the shell model, the TBRE model space is defined by a set of spherical single-particle levels labeled by the angular momentum j; the corresponding creation and annihilation operators are denoted as $a^\dagger_{jm}$ and a_{jm}. We assume the one-body Hamiltonian

$$H^{(1)} = \sum_j \epsilon_j \sum_m a^\dagger_{jm} a_{jm} \tag{1.1}$$

to be fixed with a given set of single-particle energies ϵ_j. A generic two-body Hamiltonian is built upon normalized pair creation and pair annihilation operators, $P^{(\alpha)\dagger}_{L\Lambda}$ and $P^{(\alpha)}_{L\Lambda}$,

$$H^{(2)} = \sum_{L\alpha\beta} V^{(\alpha,\beta)}_L \sum_\Lambda P^{(\alpha)\dagger}_{L\Lambda} P^{(\beta)}_{L\Lambda}, \tag{1.2}$$

where $\alpha = \{j_1, j_2\}$ is a pair index and labels L and Λ stand for the angular momentum and magnetic projection of the pair. To simplify the notation we do not include isospin labels explicitly. In the TBRE the matrix elements $V^{(\alpha,\beta)}_L = V^{(\beta,\alpha)}_L$ are real and selected at random from a Gaussian distribution centered at zero, with the variance of the off-diagonal elements doubled as compared to the diagonal elements $\langle V^{(\alpha,\beta)}_L V^{(\alpha',\beta')}_L \rangle = (\delta_{\alpha\alpha'}\delta_{\beta\beta'} + \delta_{\alpha\beta'}\delta_{\beta\alpha'})/2$.

It has been shown that the TBRE reproduces signatures of chaotic dynamics, which are given by the GOE, such as the Porter-Thomas distribution for the weights of the wave functions and the nearest level spacing distribution given by the Wigner distribution for chaotic systems [14]. Later, the application of the TBRE has been

extended to the low-energy spectra, this energy region in nuclei is dominated by regular dynamics. In order to explore the low-lying region, a many-body Hilbert space spanning all symmetry classes of states was considered [15]. The low-lying spectra in such ensembles exhibit regularities similar to those observed in real nuclei; the high probability for the zero ground-state spin is most astounding. This discovery gave a new direction in the field of random ensembles and partially motivated the main goal of this work, namely to study properties of the mean field formed in ensembles of randomly interacting nucleons. RMT can also be a tool for identifying the violation of symmetries such as time-reversal symmetry, parity, and isospin (see [16] and references therein). Another aspect of this work is the investigation of the effect of time-reversal violation in the TBRE.

This thesis is organized as follows: Chapter 2 addresses the role of time-reversal invariance in the TBRE systematics. Collective models and their signatures are introduced in Chapter 3. In Chapter 4 we present results for collective motion in systems governed by random Hamiltonians, and discuss interaction components responsible for the observed patterns. Chapter 5 is dedicated to the discussion of the SU(3) symmetry and its role in the formation of rotational modes in real as well as randomly interacting systems.

CHAPTER 2

TIME-REVERSAL INVARIANCE AND GROUND-STATE SPIN STATISTICS IN THE TBRE

2.1 Ground-state regularities in the TBRE

It has been observed in various TBRE models for both fermionic and bosonic systems that the probability for the ground state to have spin zero is enhanced [17, 6, 18]. In the TBRE the probability to observe $J = 0$ in the ground state is higher than any other spin, and is enhanced as compared with the number of states with $J = 0$ out of all possible J-configurations. In real nuclei, spin zero ground states occur in all even-even nuclei (nuclei with even number of protons and neutrons), and this is attributed to a specific component of the nucleon-nucleon interaction, namely pairing. There have been various proposals explaining the predominance of spin-zero ground states in random ensembles, [3, 16, 6] and references therein, but the full understanding of this phenomenon is still missing. It is feasible to explore the role of time-reversal invariance (T-invariance), since this symmetry is one of the ingredients needed for the formation of nucleonic Cooper pairs with zero spin.

In the spirit of the traditional shell model approach, we define a model configuration as $(j_1, j_2 \dots)^N$, where N nucleons occupy a set of single-particle levels labeled by their angular momentum j. In this thesis, unless explicitly stated otherwise, the single-particle energies are degenerate; when it is needed we also label the parity of

the single-particle levels. All calculations are done with the shell model code [19]. The size of matrices varies from ∼2,500 to 250,000 and they are diagonalized using the Lanczos algorithm. Depending on the size of the many-body space of a given system, each ensemble in this work contains from 10,000 to 500,000 random realizations.

Before turning to this issue, we would like to discuss statistics of the ground-state spin in the TBRE. We take as an example a system with N nucleons of the same kind placed in two spherical orbitals with the total angular momentum $j_1 = j_2$ and opposite parity, $l_1 - l_2 = 1$. The choice of this valence space is such that it allows us to investigate parity, as well as spin, systematics. Shown in Fig. 2.1 is the probability distribution of the ground-state spin J_{gs} and parity π for three systems $(13/2^+, 13/2^-)^6$, $(13/2^+, 13/2^-)^8$, and $(13/2^+, 13/2^-)^{10}$. In an overwhelming number of cases the ground state has positive parity, while the probability of the ground state to be of negative parity is suppressed. Spin zero is most statistically pronounced among states with positive parity. Similarly to the ground-state spin distribution, the parity distribution does not correlate with the statistical weight of states of a given parity π in the many-body space. For all considered models, the number of states with positive and negative parities is either exactly the same or of the same order. For the systems shown in Fig. 2.1, the dimensions are the following: 8,212 for both parities ($N = 6$ particles); 61,883 for negative and 61,828 for positive parities ($N = 8$ particles); 246,942 ($N = 10$ particles) for both parities. It has been shown that for systems comprised of both protons and neutrons, the parity distribution follows the trend observed in real nuclei, namely even-even random systems favor positive parity, while for odd-odd and odd-A systems the probabilities are comparable for both parities [20]. Another observed trait in this model is the appearance of the correlated spin sequences $0^+, 3^-$ and $0^+, 2^+$ with the empirical probability of finding a given sequence larger than the probability of independent events. This suggests a possible presence of octupole and quadrupole collectivity in the TBRE.

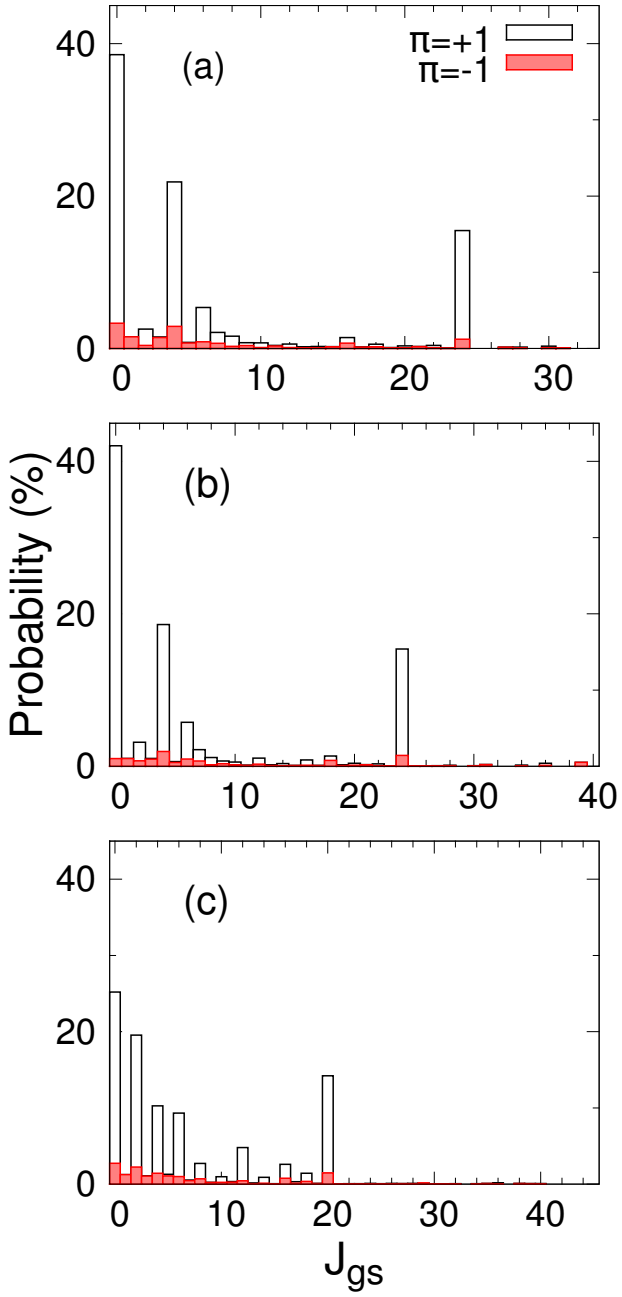

Figure 2.1: $(13/2^+, 13/2^-)^N$. The distribution of the ground state spin J_{gs} for three systems with (a) $N = 6$, (b) $N = 8$, and (c) $N = 10$ nucleons in two $j_1 = j_2 = 13/2$ orbitals. The distributions for different parity are stacked in the histogram, with non-shaded histogram showing statistics for positive parity ground state and shaded histogram showing statistics for the negative parity ground state.

2.2 External T-violation: magnetic field

Applying a magnetic field $\mathbf{B}$ is a straight forward method of breaking time-reversal invariance (T-invariance). The magnetic field also violates rotational invariance so that we can only consider the statistics of the magnetic quantum number M which is still a good quantum number. This additional part of the Hamiltonian can be expressed as

$$H_B = \sum_{a=1}^{N} g\,\mathbf{B}\cdot\mathbf{j}_a = g\,\mathbf{B}\cdot\mathbf{J}, \tag{2.1}$$

where $\mathbf{J}$ is the total angular momentum of the system, and g is the gyromagnetic ratio. The gyromagnetic ratio can be taken constant for fermions occupying a single j-shell. Without loss of generality we assume $g = -1$ and consider only $M \geq 0$. By choosing the momentum quantization axis along the $\mathbf{B}$ field we find a typical Zeeman splitting, where each eigenstate $|JM\rangle$ of the original Hamiltonian (1.2) with energy E_0 acquires an additional M-dependent contribution $E = E_0 + gBM$. Since the energy of a substate with $M = J$ is lowered the most by the Zeeman splitting, M of the ground-state coincides with J, from which this magnetic projection originates. Presented in Fig. 2.2 are statistics for the ground-state magnetic number M for $N = 6$ particles in the $j = 15/2$ orbital. As can be seen in Fig. 2.2(a), in the case with $B = 0$ the ground state has most likely the $M = 0$ ($J = 0$) projection. The probability for the ground state to have $M = 0$ drops as the magnetic field increases (Figs. 2.2(a) and (b)). The states with $M = 0$ are not affected by the field and thus their energies remain unchanged, while other states with large magnetic quantum numbers are pushed down in energy. Eventually the largest M value dominates the lower part of the spectrum.

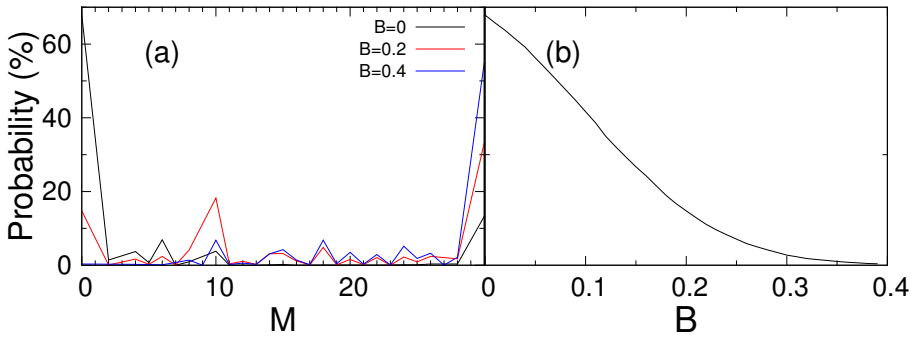

Figure 2.2: $(15/2)^6$. The effect of the external magnetic field B on the statistics of the ground state spin. (a) Distribution of the magnetic number M_{gs} for the unperturbed system ($M = J$), $B = 0$, and for two values of the magnetic field, $B = 0.2$ and $B = 0.4$. (b) Probability of $M_{gs} = 0$, corresponding to the realizations with $J_{gs} = 0$ for the unperturbed system, as a function of the magnetic field B.

2.3 Internal T-violation: one-body scalar operator

T-invariance can also be violated intrinsically. Given the three vector operators associated with a particle, $\mathbf{r}$, $\mathbf{p}$, and $\boldsymbol{\sigma}$, the simplest one-body T-odd scalar operators are

$$H_{TP} = \boldsymbol{\sigma} \cdot \mathbf{r}, \tag{2.2}$$

$$H_T = \mathbf{p} \cdot \mathbf{r}. \tag{2.3}$$

The first operator also violates parity invariance; the subscripts T and P denote symmetries broken by these operators. In the spherically symmetric potential, the single-particle wave function $\phi(\vec{r})$ is characterized by the set of quantum numbers (n, l, s, j) and takes the form

$$\phi(\vec{r}) = R_{nl}(r) \left[i^l Y_l \otimes \chi^s \right]_{jm}, \tag{2.4}$$

where a phase i^l is added to insure a conventional phase change under T-reversal. In the spherical representation the scalar product (2.2) can be written as $\boldsymbol{\sigma} \cdot \mathbf{r} =$

$\sum_{m=0,\pm1} \sigma_m r_{-m}$, with $r_m \propto rY_{1m}(\theta,\phi)$; here the subindex m indicates a change in the projection of the single-particle angular momentum (spin). It is clear from rotational symmetry that, for a single-level valence space, the effect of the operators H_{TP} and H_T could only result in a trivial shift of the whole spectrum by a constant value. Thus in order to study the T-invariance by means of the operators (2.2) or (2.3), the minimal model space should include two single-particle levels with same angular momenta j and different parity. We consider two-level models with the total momenta $j_1 = l_1 \otimes s_1$ and $j_2 = l_2 \otimes s_2$, where l_1 and l_2 are different by one and $j_1 = j_2$ since the operator H_{TP} is a scalar. In the second quantization formalism, a one-body operator $\hat{O}$ can be written as $\hat{O} = \Sigma_{kk'} \langle k|\hat{O}|k'\rangle a_k^\dagger a_{k'}$, giving the following expressions for the operators (2.2) and (2.3) acting in the two-level valence space

$$H_{TP} = iq \sum_m (a^\dagger_{j_1 m} a_{j_2 m} - a^\dagger_{j_2 m} a_{j_1 m}), \tag{2.5}$$

$$H_T = p \sum_m (a^\dagger_{j_1 m} a_{j_2 m} + a^\dagger_{j_2 m} a_{j_1 m}), \tag{2.6}$$

with real parameters $q = \mathrm{Re}|\langle j_1 m|\boldsymbol{\sigma}\cdot\mathbf{r}|j_2 m\rangle|$ and $p = \mathrm{Re}|\langle j_1 m|\boldsymbol{\sigma}\cdot\mathbf{p}|j_2 m\rangle|$. Interestingly, the expressions (2.5) and (2.6) can be "reversed" with a different choice of the phase of the single-particle wave function

$$H_{TP} = q \sum_m (\tilde{a}^\dagger_{j_1 m} \tilde{a}_{j_2 m} + \tilde{a}^\dagger_{j_2 m} \tilde{a}_{j_1 m}), \tag{2.7}$$

$$H_T = ip \sum_m (\tilde{a}^\dagger_{j_1 m} \tilde{a}_{j_2 m} - \tilde{a}^\dagger_{j_2 m} \tilde{a}_{j_1 m}), \tag{2.8}$$

where $a_{jm} = i^l \tilde{a}_{jm}$. This implies that with the addition of the operator (2.2) the Hamiltonian matrices can be chosen to be real. The effect of both operators is a transfer of a particle between two levels which have different parity. In the many-body space, the contribution of the operator (2.2) appears as a coupling of the states

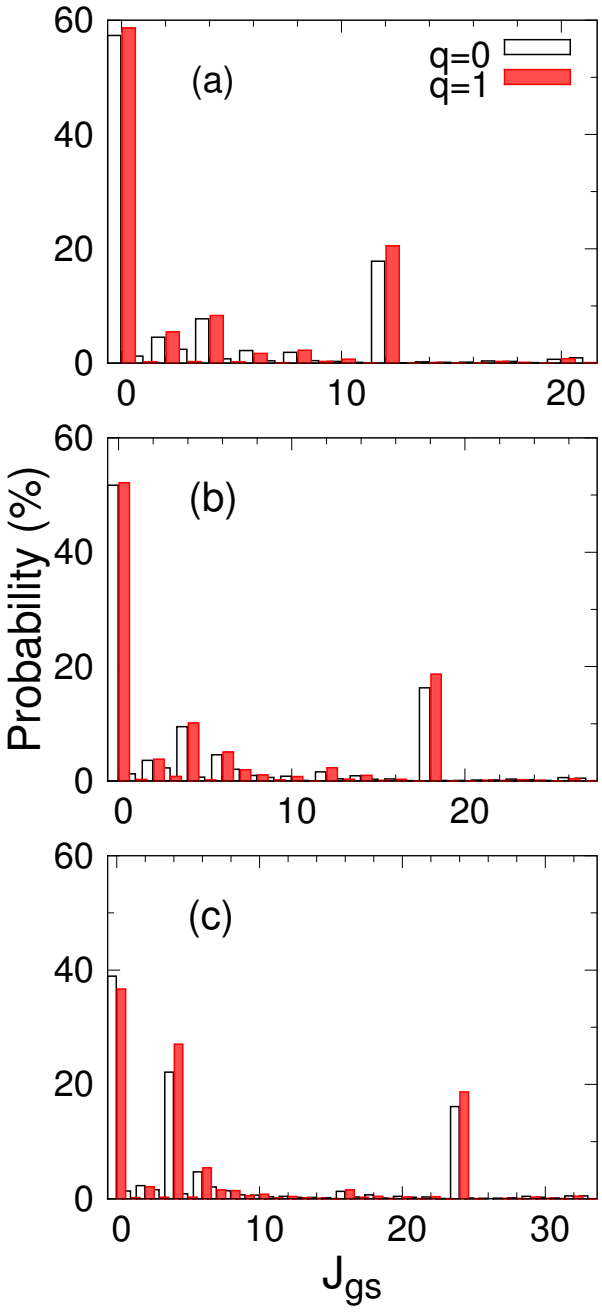

Figure 2.3: The distribution of the ground state spin J_{gs} for the T-reversal invariant TBRE, $q = 0$, and for the TBRE in the presence of the one-body T-non-invariant term (2.8), $q = 1$. Three degenerate systems were considered: (a) $(9/2^+, 9/2^-)^6$, (b) $(11/2^+, 11/2^-)^6$, and (c) $(13/2^+, 13/2^-)^6$.

with different parity and the same total angular momentum and thus the parity of each state does not have a definite value with this Hamiltonian.

Fig. 2.3 illustrates the ground-state spin statistics for the TBRE, $q = 0$, and for the TBRE with the addition of T-violation of the form of (2.8) with $q = 1$. Three degenerate two-level systems are considered with $N = 6$ nucleons placed into the orbitals $j_1 = j_2 = 9/2, 11/2, \text{and} 13/2$. As one can see from the figure, the introduction of the symmetry-breaking term does not change the g. s. spin distribution drastically. Although the two distributions are different within the statistical error for all three systems (not shown), they follow each other quite closely. As compared with the regular, T-even, TBRE, the probability of the occurrence of the $J_{gs} = 0$ state in the T-odd ensemble slightly increases for $(9/2^+, 9/2^-)^6$, while it decreases for the other two systems $(11/2^+, 11/2^-)^6$ and $(13/2^+, 13/2^-)^6$.

CHAPTER 3

COLLECTIVE MOTION IN NUCLEI

3.1 Signatures of collective motion in nuclei

In order to examine collective features in low-lying spectra which correspond to rotations, surface vibrations, and superconducting phenomena, we evaluate the expectation values of the electric multipole operators:

$$M_{\lambda\mu} = \int \rho(\mathbf{r}) r^{\lambda} Y_{\lambda\mu}(\hat{\mathbf{r}}) d^3r, \tag{3.1}$$

where $\rho(\mathbf{r})$ is the nuclear charge density and $Y_{\lambda\mu}(\hat{\mathbf{r}})$ are spherical harmonics. The operators $M_{\lambda\mu}$ can be seen as collective variables describing the mean field. This implies that the expectation values of the multipole operators between collective many-body states are enhanced. We will use the multipole operators $M_{\lambda\mu}$ in the Cartesian form, $\mathcal{M}_{\lambda\mu}$, for example, for the quadrupole operator, $\lambda = 2$, $\mathcal{M}_{2\mu} = \sqrt{\frac{16\pi}{5}} M_{2\mu}$.

The reduced transition probability from a state $|J_i M_i\rangle$ to a state $|J_f M_f\rangle$ is defined by the off-diagonal matrix elements of the multipole operator

$$B(E\lambda, J_i \to J_f) = \sum_{\mu, M_f} |\langle J_f M_f | \mathcal{M}_{\lambda\mu} | J_i M_i \rangle|^2, \tag{3.2}$$

where $|JM\rangle$ denotes a many-body state with a magnetic projection M, and all remaining quantum numbers including angular momentum are denoted by J. We should

note that the standard definition of the reduced transition probability involves multipole operators in the spherical form (3.1). The overall normalization of the reduced transition rates is given by the transition strength

$$S_\lambda(J_i) = \sum_{J_f} B(E\lambda, J_i \to J_f) = \langle J_i M_i | \sum_\mu \mathcal{M}^\dagger_{\lambda\mu} \mathcal{M}_{\lambda\mu} | J_i M_i \rangle. \tag{3.3}$$

The shape of a state is described by the diagonal elements of the multipole operator (or multipole moments)

$$\mathcal{Q}_\lambda(J) = \langle JM = J | \mathcal{M}_{\lambda 0} | JM = J \rangle. \tag{3.4}$$

In this work we only briefly touch on the subject of collectivities other than quadrupole, thus for convenience the subscript λ in Eqs. (3.3) and (3.4) is omitted for $\lambda = 2$.

3.2 Models of nuclear rotations

A static deformation of the nuclear surface opens a possibility for rotations in nuclei. In this chapter we describe both geometric and algebraic approaches to rotational motion. The geometric, or rigid rotor model is built up by quantization of the liquid drop model. We briefly summarize some of the well-known properties of the rotor model with an emphasis on the axially symmetric rotor. Formation of a deformed mean field in the basis of the spherical shell model is illuminated in the algebraic Elliot SU(3) model. In the second part of this chapter we present the SU(3) model and its comparison with the rigid rotor.

3.2.1 Rigid rotor model

Parametrization of the surface of the nucleus is a starting point in describing nuclear shapes. The conventional surface parametrization is given in terms of spherical harmonics and expansion coefficients $\alpha_{\lambda\mu}$

$$R(\theta, \phi) = R_0 \left(1 + \sum_{\lambda=0}^{\infty} \sum_{\mu=-\lambda}^{\lambda} \alpha^*_{\lambda\mu} Y_{\lambda\mu}(\theta, \phi) \right), \tag{3.5}$$

where R_0 is the radius of a spherical nucleus of the same volume. The $\lambda = 0$ term corresponds to a change of volume; taking into account the incompressibility of the nucleus, this term can be chosen to compensate for a change of volume in other multipole modes. The $\lambda = 1$ term corresponds to a translation of the center of mass. Thus, the first relevant term is the quadruple term; $\lambda = 2$, it is the dominant mode in nuclei and we will discuss it in more details.

For the quadruple deformation, three parameters out of five ($\lambda = 2, \mu = \pm 2, \pm 1, 0$) determine the orientation of the nucleus in the laboratory frame and can be related to three Euler angles. Hill-Wheeler coordinates α and β can be conveniently taken as $\alpha_{20} = \beta \cos\gamma$ and $\alpha_{22} = \alpha_{2-2} = \beta \sin\gamma/\sqrt{2}$. These two parameters define the quadrupole operator, which is a multipole operator (3.1) of order $\lambda = 2$. The variable β ($\beta > 0$) describes the overall level of deformation, and the mean field is spherical if $\beta = 0$. The variable γ indicates the deviation from axial symmetry, see Fig. 3.1. The Hill-Wheeler parameters define the quadrupole operator Limits $\gamma = 0°, 120°, 240°$ correspond to prolate (cigar-like) shapes. The deformation is oblate (pancake-like) for $\gamma = 60°, 180°, 300°$. (There is an alternative convention with $\beta > 0$ for prolate nuclei and $\beta < 0$ for oblate nuclei.) An interesting phenomenon is observed in stably deformed nuclei: the overwhelming majority of such nuclei have a prolate shape in the ground state.

In the rigid rotor model one assumes an adiabatic approximation, namely, that the internal structure of the nucleus does not change leaving only the extrinsic, or rotational, degrees of freedom [2]. The rotational Hamiltonian

$$H_{\rm rot} = \sum_{k=1}^{3} \frac{J_k^2}{2\mathcal{L}_k} \tag{3.6}$$

is then characterized by three moments of inertia along the principal body-fixed axes $\mathcal{L}_1$, $\mathcal{L}_2$, and $\mathcal{L}_3$.

The triaxial rotor (a rotor with all three moments of inertia $\mathcal{L}_i$ different) possesses a symmetry of the discrete D_2 group [2, 21], which restricts the possible values of the

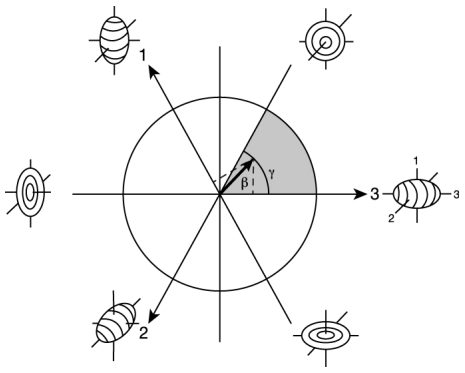

Figure 3.1: Quadruple deformations in the $\beta\gamma$ plane. From [1]

angular momentum J. The allowed values can be found from the irreducible representations. The group consists of four elements: the unit transformation and three rotations by π, $R_i(\pi)$ with $i = 1, 2, 3$, around three principal body-fixed axes $1, 2, 3$. These operators commute, and thus can be diagonalized simultaneously. Taking into account that eigenvalues of these operators can be either +1 or -1 and that $r_i = r_j r_k$ for $i \neq j \neq k$ (or $R_i(\pi) = R_j(\pi)R_k(\pi)$ for $i \neq j \neq k$), there are four possible one-dimensional irreducible representations $(r_1\, r_2\, r_3) : (+++), (+--), (-+-), (--+)$. The irreducible representation of interest in this thesis is $(+++)$. In this representation there are $J/2+1$ states for even J and $(J-1)/2$ states for odd J, e.g. 0, 2(2), 3, 4(3), 5(2)... [21].

The two tensors, the moment of inertia and the quadrupole moment, describe triaxial nuclei; these quantities are correlated. The quadrupole moment is defined by the Hill-Wheeler parameters γ and β and is independent of the Hamiltonian. The correlation between these two tensors is model-dependent. The standard model of a triaxial nucleus, the Davydov-Filippov model [22], assumes the irrotational-flow values:

$$\mathcal{L}_k = \frac{4\hbar^2}{3E_{\mathrm{R}}} \sin^2\left(\gamma - \frac{2\pi}{3}k\right), \quad k = 1, 2, 3, \tag{3.7}$$

where E_{R} defines the energy scale and is inversely proportional to β^2. For realistic

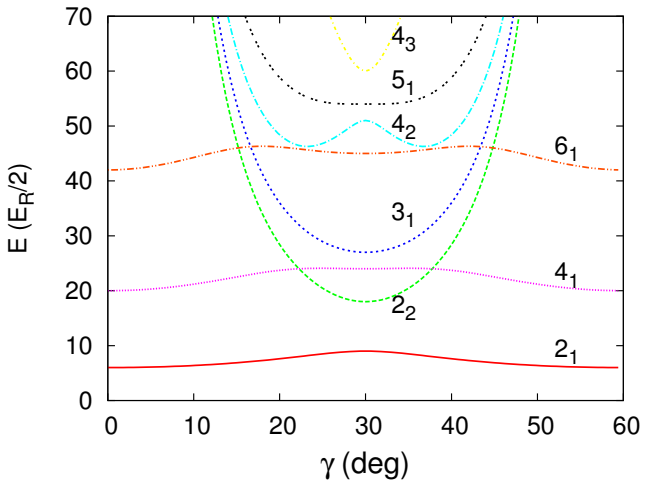

Figure 3.2: Low-lying spectrum of a triaxial rotor with the irrotational-flow moments of inertia. The energy scale is given by the parameter $E_{\rm R}$ defined in Eq. (3.7).

nuclei $E_{\rm R}$ is given by the total mass and the nuclear density, so we treat it as a parameter which substitutes for β. Moments of inertia in the limit of irrotational flow are higher than the observed moments. An alternative rigid-body limit results in lower predictions; the actual measured moments of inertia lies in between these two limits $\mathcal{L}^{\rm irr} < \mathcal{L}^{\rm exp} < \mathcal{L}^{\rm rid}$.

In the axially symmetric case ($\gamma = 0°$), the projection of the angular momentum onto the symmetry axis 3, K, (Fig. 3.3) is an additional conserved quantum number. The energy levels characterized by the same K form a rotational band. For the ground state band, $K = 0$, the total angular momentum J can take only even values and the excitation energies become $E(J) = J(J+1)E_{\rm R}/2$. The onset of triaxiality only slightly changes the positions of levels of a symmetric top, $2_1, 4_1, 6_1$, however the new levels 2_2, 3_1, 4_1, 5_1 appear low in the spectrum, see Fig. 3.2. In this notation for states, the subscript refers to the order of a state among other states of the same spin. The energy is the same for prolate ($\gamma = 0° \ldots 30°$) and oblate ($\gamma = 30° \ldots 60°$) deformations with the same β.

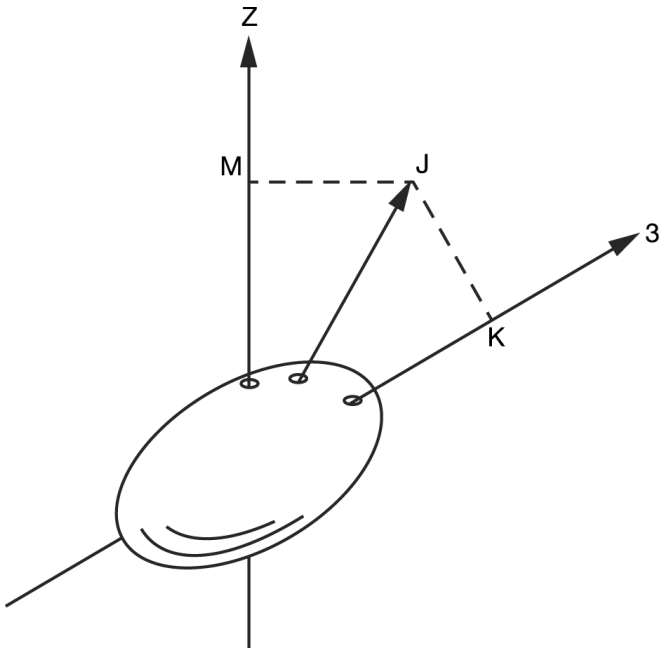

Figure 3.3: Projections of the total momentum J onto the symmetry axis (body-fixed frame), K, and z axis (laboratory frame), M. From [2]

Most features of the irrotational flow model has been discussed in Ref. [22]; here we review some specifics which are relevant to this work. For an arbitrary γ the energies are determined by eigenvalues of matrices with dimensionality $J/2+1$ for even J and of order $(J-1)/2$ for odd J. For two states of interest in our work 2_1 and 2_2, the result is analytic

$$E(2_{1,2}) = \frac{3E_{\rm R}}{4}\frac{9 \mp 3\sqrt{9-8\sin^2(3\gamma)}}{\sin^2(3\gamma)}. \tag{3.8}$$

The $E2$ gamma transitions provide a strong evidence of rotational collective dynamics. For our schematic studies we assume that the scale of the quadrupole transitions is given by the intrinsic quadrupole moment Q, which depends on the deformation parameter β. Spherically symmetric nuclei with $\beta = 0$ have zero quadrupole moment $Q = 0$, while $Q > 0$ for prolate nuclei, and $Q < 0$ for oblate nuclei. Measured in the laboratory frame, the quadrupole moment $\mathcal{Q}(2_1)$ has a sign opposite to that in the

body-fixed frame Q:

$$\mathcal{Q}(2_1) = -\frac{6Q\cos(3\gamma)}{7\sqrt{9-8\sin^2(3\gamma)}}. \tag{3.9}$$

Notice that both $J = 2$ states of the triaxial rotor have equal in magnitude and opposite in sign values of the quadrupole moment, $\mathcal{Q}(2_1) = -\mathcal{Q}(2_2)$, which occurs because the quadrupole operator is traceless. The transition strength (3.3) for the $E2$ transitions from the $J = 0$ ground state is saturated by the two $J = 2$ states: $B(E2, 0_{gs} \to 2_1) + B(E2, 0_{gs} \to 2_2) = Q^2$. The explicit values for rates are

$$B(E2, 0 \to 2_{1,2}) = \frac{Q^2}{2}\left[1 \pm \frac{3-2\sin^2(3\gamma)}{\sqrt{9-8\sin^2(3\gamma)}}\right]. \tag{3.10}$$

The near saturated transition strength and non-zero quadrupole moment are good evidences for rotational collectivity. Triaxiality, however is hard to detect since the $0_{gs} \to 2_1$ transition dominates over the $0_{gs} \to 2_2$ transition, comprising between 93% and 100% of the sum. The rate between the 2_1 and 2_2 states is only strong for large triaxiality

$$B(E2, 2_2 \to 2_1) = \frac{2Q^2}{7}\frac{\sin^2(3\gamma)}{9-8\sin^2(3\gamma)}. \tag{3.11}$$

In the Davydov-Filippov model discussed above the asymmetry (triaxiality) is incorporated in the rotational Hamiltonian, for which an assumption concerning the moments of inertia has to be made. An alternative, "two-band", approach to the description of triaxiality for nuclei with a small $\Delta K = 2$ mixing has been offered recently [23, 24]. This approach allows one to find the deformation parameter γ without an adherence to any form of the moments of inertia. Motivated by this two-band prescription, we propose a method for identifying triaxiality based on the characteristics of the 2_1 and 2_2 states. Our method is described in Ch. 4, the application of this method to the detection of triaxiality in random ensembles and the quadrupole-quadrupole interaction are presented in Chs. 4 and 5, correspondingly.

3.2.2 Elliot SU(3) model

Eight generators, three angular momentum operators L_μ with $\mu = 0, \pm 1$ (tensors of rank one) and five quadrupole operators ${\mathcal{M}'}_{2\mu}$ with $\mu = 0, \pm 1, \pm 2$ (tensors of rank two), form the Lie algebra of the SU(3) group [25]. The SU(3) quadrupole-quadrupole (QQ) Hamiltonian

$$H_{\mathrm{SU(3)}} = -\sum_{\mu} {\mathcal{M}'}^{\dagger}_{2\mu} {\mathcal{M}'}_{2\mu} \tag{3.12}$$

is an invariant of the SU(3) group since it commutes with the group generators.

The group irreducible representations (or multiplets) are labeled with a set of two integers (λ, μ). The representations are finite dimensional and the group is compact [26], with dimensionality

$$\dim(\lambda, \mu) = 1/2(\lambda + 1)(\mu + 1)(\lambda + \mu + 2). \tag{3.13}$$

The states in each multiplet can be characterized by a quantum number K':

$$K' \geq 0, K' = \overline{\mu}, \overline{\mu} - 2 \ldots, \tag{3.14}$$

where $\overline{\mu} = \min(\lambda, \mu)$. The quantum number K' is not an eigenvalue of any operator, it provides a connection with the angular-momentum subgroup. For each multiplet (λ, μ) the angular momentum L takes values:

$$L = \begin{cases} K', K' + 1 \ldots K' + \overline{\lambda} & \text{for } K' > 0 \\ \overline{\lambda}, \overline{\lambda - 2} \ldots & \text{for } K' = 0, \end{cases} \tag{3.15}$$

with $\overline{\lambda} = \max(\lambda, \mu)$.

Within a given multiplet, the structure of the spectrum and transition rates are similar to those of a rigid rotor. For each multiplet (λ, μ) a finite-size rotational band emerges with energies:

$$E_{\mathrm{SU(3)}} = -S(\lambda, \mu) + 3L(L + 1), \tag{3.16}$$

Table 3.1: Values of the SU(3) quantum number K', angular momentum L, total momentum J, and Casimir operator $S(\lambda, \mu)$ for each SU(3) multiplet for two particles in the *sd*-shell.

	(4,0)	(2,1)	(0,2)
K'	0	1	0
L	0,2,4	1,2,3	0,2
$J = L \oplus S$	0,2,4	0,1(2),2(3),3(2),4	0,2
$E_{\mathrm{SU(3)}}$	112,94,52	58,46,28	40, 22

where

$$S(\lambda, \mu) = 4[\lambda^2 + \mu^2 + \lambda\mu + 3(\lambda + \mu)] \tag{3.17}$$

is the expectation value of the SU(3) Casimir operator.

The number K' indicates how to construct SU(3) states with a definite angular momentum L. K' is close in its meaning to the quantum number K discussed in the rotor model, and these numbers are identical in the asymptotic limit of large λ or μ. The formal equivalence between the rigid-rotor and SU(3) models occurs for representations with $2\lambda + \mu \gg 1$ and $L \ll 2\lambda + \mu$, see [27].

Systems in the SU(3) model are triaxial if both λ and μ have non-zero values. The axial symmetry appears in so-called stretched cases, when one of the quantum numbers is zero; in this case the matrix elements of the quadrupole operator can be expressed analytically [26]. Slightly away from stretched cases for $\lambda \gg \mu$ (for large number of particles and away from half-occupied cases), the structure is analogous to that of a triaxial rotor with the triaxiality Hill-Wheeler parameter $\gamma^2 \simeq \mu/(2\lambda + \mu)$ [27].

The Elliot SU(3) model [7] provides a link between the collective rigid-rotor model and the spherical shell model. A good approximation to the shell-model mean field is the harmonic oscillator potential. The three-dimensional isotropic harmonic oscillator is invariant under the SU(3) symmetry. In this case the SU(3) numbers λ

and μ represent a difference in the number of oscillatory quanta between z-x and x-y directions respectively.

The ground state multiplet (λ, μ) for any given shell-model configuration is easy to determine by examining particle distributions and the resulting distribution of oscillator quanta between three cartesian directions (see Appx. B). All possible SU(3) representations can be obtained in a similar manner. The list of the SU(3) representations for N particles can be also generated as a tensor product of a single-nucleon SU(3) representation $(n, 0)$, where n is the order of an oscillatory shell. The Pauli exclusion principal should be additionally enforced, which excludes some of the representations. Nevertheless the tensor-product method can be illustrative as we show for the $(1s, 0d)^2$ configuration (two particles in the sd shell). The coupling of two stretched representations $(\lambda_1, 0)$ and $(\lambda_2, 0)$ is trivial [28]:

$$(\lambda_1, 0) \otimes (\lambda_2, 0) = (\lambda_1 + \lambda_2, 0) \oplus (\lambda_1 + \lambda_2 - 2, 1) \oplus (\lambda_1 + \lambda_2 - 4, 2) \dots . \tag{3.18}$$

For $N = 2$ nucleons in the $n = 2$ shell, the product decomposition is $(2, 0) \otimes (2, 0) = (4, 0) \oplus (2, 1) \oplus (0, 2)$. The quantum numbers for each SU(3) band are summarized in Tab. 3.1. Possible values of K' and L are generated according the the rule (3.14).

There is a symmetry between quantum numbers λ and μ; for a less than half-occupied oscillator shell, the ground state band (λ, μ) has $\lambda > \mu$ and thus the prolate intrinsic shape. Due to the exact particle-hole symmetry in the SU(3) model, a system with the same number of holes has a ground state multiplet (μ, λ), and its intrinsic shape is oblate [27].

The SU(3) QQ Hamiltonian (3.12) is a special case of the QQ Hamiltonian:

$$H_{\mathrm{QQ}} = -\sum_{\mu} \mathcal{M}^{\dagger}_{2\mu} \mathcal{M}_{2\mu}, \tag{3.19}$$

which is defined in terms of the quadrupole operator $\mathcal{M}_{2\mu}$ from Eq. 3.1 with $\lambda = 2$, rather than the SU(3) quadrupole operator $\mathcal{M'}_{2\mu}$; these operators coincide within one

oscillatory shell. The QQ Hamiltonian is central in our study of collective motion in the two-body random ensemble in Ch. 4. We also closely investigate the QQ spectrum in Ch. 5.

3.3 Vibrations and boson model

Nuclei exhibit various vibrational modes in different mass and energy regions. We concentrate on surface vibrations around a spherical shape, which are relevant to our discussion of the structure of the low-energy levels in the shell model. In the simple model of surface vibrations, the Hamiltonian is taken to be that of the harmonic oscillator, where the parameters $\alpha_{\lambda\mu}(t)$ (Eq. 3.5) serve as collective coordinates. In quantized form the Hamiltonian can be written in terms of bosonic creation and annihilation operators [2]. The equidistant excitation spectrum is built up by vibrational quanta, or phonons. For quadrupole oscillations the first excited one-phonon state is non-degenerate, with spin $J = 2$ (Fig. 3.4).

Because of their bosonic nature, two quadrupole phonons can couple only into even total spin $0, 2,$ and 4. Thus, the second excited state is 3-fold degenerate. Multi-phonon states have been observed in spherical nuclei, although the degeneracy of the multiplets is lifted due to residual interactions. The *yrast* states (states of the lowest energy for a given spin) are formed by n phonons uniquely coupled to the maximum possible spin $J = 2n$. Any n-phonon state can decay via an $E2$ transition only into a $(n-1)$-phonon state. These two conditions define a ratio of the transition rates between the yrast states $J_i = 2n$ and $J_f = 2(n-1)$ in a simple way [2]:

$$\sum_{J_f} B(E2, J_i \to J_f) = nB(E2, 2_1 \to 0_{gs}). \tag{3.20}$$

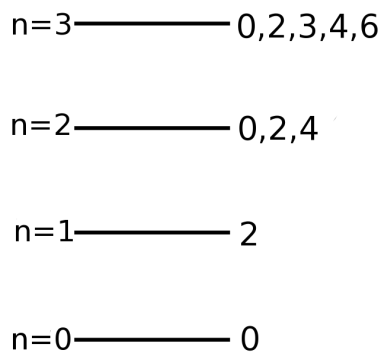

Figure 3.4: Low-lying levels of the quadrupole harmonic vibrator.

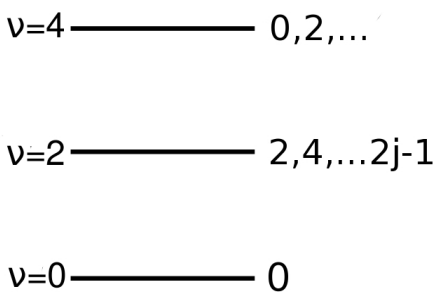

Figure 3.5: Low-lying spectrum of the pairing Hamiltonian on a single j orbital in the limit $N \ll \Omega$.

3.4 Pairing and seniority model

Pairing is an important part of the nucleon-nucleon interaction. Short-range pairing and long-range quadrupole-quadrupole interactions lead to two competing collective modes. Their interplay affects many aspects of nuclear structure, from binding energies to collective motion.

In the case of pure pairing on a single j-level, $V_{L=0}^{(\alpha,\beta)} = -1$ and $V_{L\neq 0}^{(\alpha,\beta)} = 0$ in the Hamiltonian (1.2), and the seniority model introduced by Racah [29, 30] is a useful tool. The seniority scheme allows one to classify states according to the SU(2) symmetry group. The group is formed by the so-called quasispin operators S^+, S^-, S_z related to the particle number operator and pair creation and annihilation operators: $S^+ = \sqrt{\Omega/2}P_{00}^{(\alpha)\dagger}$, $S^- = \sqrt{(\Omega/2}P_{00}^{(\alpha)}$ and $S_z = N/2 - (2j+1)/4$, where $\Omega = 2j + 1$ [31, 1]. The number of unpaired particles ν, or seniority, is a conserved quantity in the pure paring model. The importance of the seniority scheme in realistic nuclei comes with the realization that in many cases the interactions conserve seniority. For example, any one- and two-body interactions preserve seniority on a singe level with $j \leq 7/2$ [32].

For the pairing Hamiltonian, the ground state has zero seniority; the first excited state is obtained by breaking one pair. The eigenvalues of the pure pairing Hamiltonian are $E(N,\nu) = -(N-\nu)(\Omega-\nu-N+2)/4$. In the limit of $N \ll \Omega$ the spectrum becomes equidistant, see Fig. 3.5. The yrast states 2_1 and 4_1 are degenerate, and thus $R_{42} = 1$.

The seniority scheme simplifies calculations of matrix elements by allowing one to use the Wigner-Eckart theorem in the quasi-spin space, see Appx. A. The application practical for our study concerns quadrupole transition rates between 0_{gs} ($\nu = 0$) and 2_1 ($\nu = 2$) states,

$$B(E2, 2_1 \to 0) = B_0 \frac{1}{5} \frac{2N(\Omega - N)}{\Omega(\Omega - 2)}, \tag{3.21}$$

and between two $\nu = 2$ states, 4_1 and 2_1,

$$B(E2, 4_1 \to 2_f) = 5B_0 \left(\frac{2(2N - \Omega)}{(4 - \Omega)} \right)^2 \left\{ \begin{array}{ccc} 2 & 4 & 2 \\ j & j & j \end{array} \right\}^2, \tag{3.22}$$

where the latter transition is defined in terms of the Wigner 6-j symbol; the derivation of this transition is given in Appx. A. The proportionality coefficient B_0 includes the radial and spin parts of the expectation value of the quadrupole operator.

Recently an exact numerical treatment of pairing has been proposed for realistic model spaces with many valence levels [33]. The method consists of introducing a quasispin formalism for each level; the seniority number for each level, as well as the total seniority, is conserved by the pairing interaction. This approach greatly reduces the space for the shell-model diagonalization, with other residual interactions being treated perturbatively.

3.5 Collective observables

In the search for collective realizations we select a set of quantities that convey most of the information about collective structures: the reduced transition rate (3.2), the multipole moments (3.4), and the transition strength (3.3). In order for these parameters to be scale independent, we normalize them assuming minimal model dependence. This is described in what follows.

The total transition strength (3.3) from a given state J provides a convenient normalization to assess the fractional collectivity of the transition

$$b(E\lambda, J_i \to J_f) = B(E\lambda, J_i \to J_f)/S_\lambda(J_i). \tag{3.23}$$

The shape of a state is described by its multipole moment (3.4). The mean field with a stable deformation opens a possibility for nuclear rotations. A rotational spectrum (band) emerges for every fixed intrinsic shape. The intrinsic shape is characterized by the body-fixed (intrinsic) multipole moments Q_λ. In a perfect rotor these intrinsic

moments are the same for all states in the band. For the ground state band of interest, these moments define the transition strength $S_\lambda(0_{gs}) = Q_\lambda^2$. Within a given band the intrinsic moments determine the lab-frame observables in Eqs. (3.2) and (3.4). In the axially symmetric case the quantum number K (a projection of the angular momentum onto the body-fixed symmetry axis) is conserved. Then for each rotational K-band the relations between the observables in the lab frame and in the intrinsic frame are expressed via Clebsch-Gordan coefficients,

$$\mathcal{Q}_\lambda(J) = Q_\lambda C^{JJ}_{\lambda 0,JJ} C^{JK}_{\lambda 0,JK} \tag{3.24}$$

and

$$B(E\lambda, J_i \to J_f) = Q_\lambda^2 \left| C^{J_f K}_{\lambda 0,J_i K} \right|^2 . \tag{3.25}$$

The limit of an axially symmetric rotor provides a convenient normalization of the multipole moments. In this work, instead of $\mathcal{Q}_\lambda(J)$ we quote a normalized intrinsic moment

$$q_\lambda(J) = \frac{Q_\lambda(J)}{\sqrt{S_\lambda(0_{gs})}}, \tag{3.26}$$

where

$$Q_\lambda(J) = \frac{\mathcal{Q}_\lambda(J)}{C^{JJ}_{\lambda 0,JJ} C^{J0}_{\lambda 0,J0}}, \tag{3.27}$$

which is computed as if the state is a member of the $K = 0$ rotational ground state band.

The relation between the quadrupole moment of the 2_1 state in the lab frame and in the intrinsic frame is $\mathcal{Q}(2_1) = -2/7\, Q(2_1)$. For an axially symmetric rotor the transition strength is saturated by a single transition $b(E2, 0_{gs} \to 2_1) = 1$ with $q(2_1) = 1$ for prolate or $q(2_1) = -1$ for oblate shapes.

We normalize the multipole transition strength $S_\lambda(J)$ in (3.3) to the maximum possible value that it can have in a given valence space. For $\lambda = 2$ the QQ Hamiltonian (3.19) establishes the maximum value of $S(J)$. The eigenstate energy of the QQ

Hamiltonian coincides with the transition strength for that state: $E_{\mathrm{QQ}}(J) = -S(J)$. Thus, the absolute value of the QQ Hamiltonian ground state energy $E_{\mathrm{QQ}}(0_{gs})$ is the maximum possible value of the transition strength $S(J)$ in a given model space with a given structure of the quadrupole operator. We thus define a relative transition strength as

$$s(J) = \frac{S(J)}{|E_{\mathrm{QQ}}(0_{gs})|}. \tag{3.28}$$

The collective structure can further analyzed for a sequence of states with spins 0, 2 and 4. The types of collective modes can be classified by the ratio of the excitation energies measured relative to the energy of the 0_{gs} state

$$R_{42} = \frac{E(4_1)}{E(2_1)}, \tag{3.29}$$

where the states are additionally denoted by a subscript indicating an order of the excited state. This ratio is 1 for pairing, 2 for vibration, and 10/3 for rotation. The deexcitation probability ratio

$$B_{42} = \frac{B(E2, 4_1 \to 2_1)}{B(E2, 2_1 \to 0_{gs})} \tag{3.30}$$

gives another measure which is nearly 0 for pairing, 2 for vibrational mode, and ≈1.43 for rotational motion. In the QQ Hamiltonian, R_{42} and B_{42} have values close to those of an axially symmetric rotor; their values for systems considered in this work are listed in Tab. 5.1.

To summarize, for all models we use the dimensionless variables defined in Eqs. (3.23), (3.26), and (3.28); to shorten notation we define $b \equiv b(E2, 0_{gs} \to 2_1)$, $q \equiv q(2_1)$, and $s \equiv s(0_{gs})$. For collective models of pairing, rotations, and vibrations $b \approx 1$. We refer to a realization with $b > 0.7$ as *collective* and with $b < 0.3$ as *non-collective*. The quadrupole moment q allows us to separate different collective modes: $q \approx \pm 1$ for rotations, and it is nearly zero for vibrations or superconducting paired states. In what follows we identify collective realizations with $q > 0.7$ as prolate

and those with $q < -0.7$ as oblate. For rotations, the relative transition strength s is related to the square of the intrinsic moment, and thus it is associated with the Hill-Wheeler deformation parameter β^2 measured relative to the maximum possible value in a given model space. In analogy with the SU(3) group, the relative transition strength s can be thought to represent the expectation value of the Casimir operator which identifies the irreducible representation of the ground state band. In cases where $s \approx 1$ the ground state band structure is close to that of the QQ Hamiltonian.

CHAPTER 4

MEAN FIELD IN THE TBRE AND ITS PROPERTIES

4.1 The single j level model

4.1.1 Quadrupole collectivity

We begin our discussion of collectivity in the TBRE with single j level models. Starting from the original paper [15] the single j level with identical nucleons has been at the center of numerous investigations; a good summary may be found in the following reviews [3, 5, 6, 34]. With many issues understood and with still unanswered questions, the single j model remains an important exploratory benchmark. The model, while simple, has a number of particularly attractive features which can be of both advantage and disadvantage: the Hamiltonian is defined with a small number of parameters; apart from an overall normalization constant, the multipole operators are uniquely defined; a special role is played by the quasispin SU(2) group; and the particle-hole symmetry is exact [35].

In the TBRE the number of realizations with the ground-state spin $J_{gs} = 0$ is disproportionally large, so in search of collectivities we always select realizations with $J_{gs} = 0$. With the exception of the ground state labeled as 0_{gs}, we denote the low-lying states by the value of their spin with an identifying subscript. The subscript is given in bold if it refers to the absolute order of a given state among all states with different spins. Throughout this thesis we give probabilities of finding realizations with certain

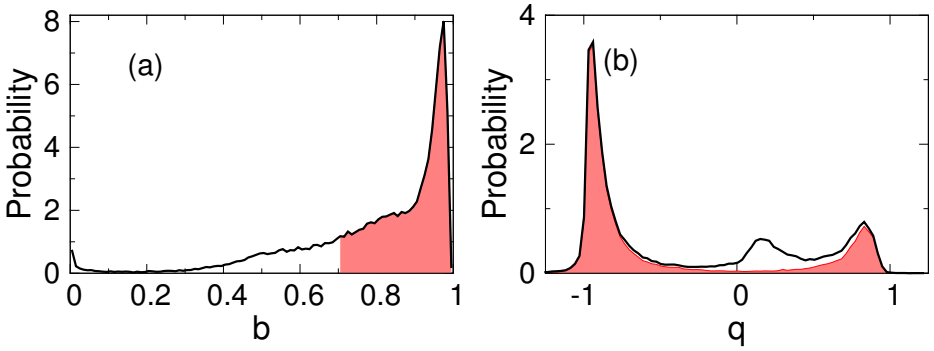

Figure 4.1: $(19/2)^6$. (a) The distribution of the fractional collectivity b. (b) The distribution of the intrinsic quadrupole moment q. Only realizations with the $0_{gs}, 2_{\mathbf{1}}$ spin sequence are included in both panels. There are 10.4% of such realizations. The 7.8% of collective realizations ($b > 0.7$) are shaded.

features; these probabilities are always quoted as a percentage of the total ensemble, however, all probability distribution plots are normalized to unit area.

We address the quadrupole collectivity in Fig. 4.1. Here the results for a system with 6 nucleons in a single $j = 19/2$ level are presented; we refer to this system as $(19/2)^6$. We select the 10.4% of random realizations where the 0_{gs} state is followed by the $2_{\mathbf{1}}$ state. The distribution of the fractional collectivity $b \equiv b(E2, 0_{gs} \to 2_1)$ in Fig. 4.1(a) points to a highly collective nature of the quadrupole transition $0_{gs} \to 2_{\mathbf{1}}$. Most of realizations with 0_{gs} and $2_{\mathbf{1}}$ are collective ($b > 0.7$), their fraction is 7.8% from the total number of samples (shaded). This collectivity is not a statistical coincidence. The system $(19/2)^6$ has 1242 J-states, among them there are 10 states with $J = 0$ and 23 with $J = 2$, thus statistically the chance to see the $0_{gs}, 2_{\mathbf{1}}$ spin sequence among all other possible outcomes is only 0.015%. The large collectivity for the transition between these two states is even more unlikely statistically. Given that the transition strength is shared among 23 $J = 2$ states, and the chance of $b(E2, 0_{gs} \to 2_1) > 0.7$ is of the order of 1 in 10^7.

There are two peaks of prolate and oblate deformations in the distribution of the quadrupole moment for collective realizations in this system, see Fig. 4.1(b).

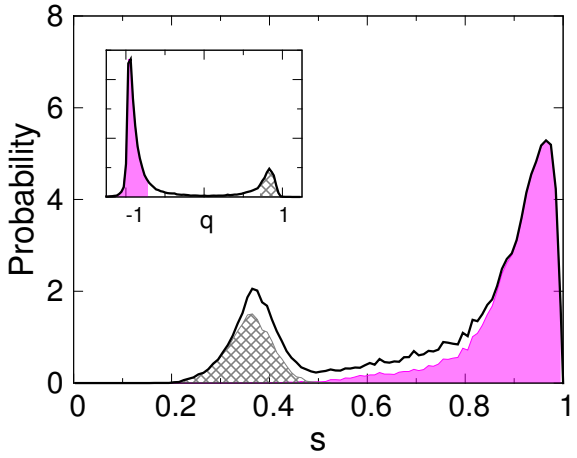

Figure 4.2: $(19/2)^6$. The distribution of the relative transition strength s for the collective realizations (shaded area in Fig. 4.1). The quadrupole moments shown in the inset are separated according to the shapes into prolate $q > 0.7$ and oblate $q < -0.7$ deformations, shaded with pattern and uniform color, respectively. The fraction of oblate cases is 5.2% and of prolate cases is 1.3% from the total number of random realizations.

For most of the collective realizations the magnitude of the quadrupole moments is consistent with the value for the axially deformed rigid rotor ($q \approx 1$). The collective realizations are further explored in Fig. 4.2, where the distribution of the relative transition strength s is shown, with the oblate ($q < -0.7$) and prolate ($q > 0.7$) cases shaded with different patterns. As one can see from Fig. 4.1(b), the shape of the ground state is most likely to be oblate. The relative transition strength s for the oblate samples is close to the maximum possible value in this model space $s \approx 1$, thus for these realizations the ground state band structure is similar to that of the QQ Hamiltonian. The same sign of deformation is predicted for this system by the QQ Hamiltonian (Tab. 5.1).The summary of the data on the QQ Hamiltonian for all models discussed in this thesis is presented in Chapter 5. In about one out of four collective cases the prolate mean field emerges. These systems are less deformed, with $s \approx 0.37$.

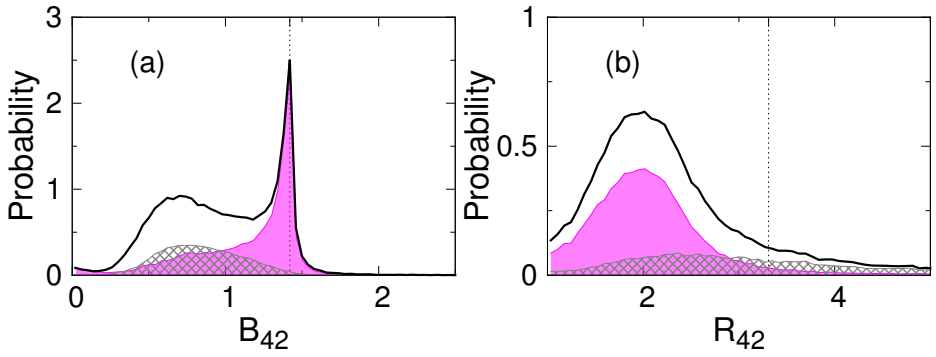

Figure 4.3: $(19/2)^6$. (a) The distribution of the deexcitation ratio B_{42} defined in Eq. (3.30). (b) The distribution of the excitation energy ratio R_{42} defined in Eq. (3.29). The distributions are comprised of 13.6% of realizations that have the 0_{gs}, 2_1, 4_1 sequence with $b > 0.7$, where the 2_1 state is not higher than the fourth excited state, and $E(4_1) > E(2_1)$. The prolate and oblate cases, which appear in the ensemble with probabilities 3.3% and 7.1%, respectively, are shaded with the same patterns as in Fig. 4.2. The values of B_{42} and R_{42} for the QQ Hamiltonian listed in Tab. 5.1 are marked with the vertical grid lines.

We slightly modify our selection of samples in Fig. 4.3 choosing collective ones that have states 2_1 and 4_1, with the 2_1 state not higher than the forth excited state and the 4_1 state above it. The behavior of the deexcitation ratio B_{42} in 3.30 is shown in Fig. 4.3(a). We use the same shading for prolate and oblate realizations as in Fig. 4.2. For this system values of the deexcitation ratio can be obtained analytically for the rotational, vibrational, and pairing limits as discussed in Sec. 3. For all collective models with rotations B_{42} is close to the rotor value of 1.4; the vibrational model gives $B_{42} = 2$; for the pairing Hamiltonian in the $(19/2)^6$ model $B_{42} = 0.15$. The collective oblate realizations comprise a peak around the rotational value of $B_{42} = 1.43$. There is an extended shoulder in the distribution for prolate realizations with a peak near $B_{42} \approx 0.8$. It is likely that in weakly deformed prolate instances (with the lower value of s) the rotational structure is more fragmented, and therefore the 4_1 state is not purely rotational. The distribution of the ratio of the excitation energies R_{42}, see Fig. 4.3(b), seems to contradict the rotational limit. For

most of the collective realizations the values of this ratio fall between the pairing limit of 1 and the vibrational limit of 2, while in the rotational limit this ratio is 3.3. This discrepancy has been reconciled in Ref. [15] with the observation that the rotational behavior emerges in the ensemble-averaged excitation energies; this is also expected from the geometrical chaoticity arguments [17]. Excitation energies are too sensitive to non-collective features, and this leads to large fluctuations of R_{42}. The experimental observations of realistic nuclei also show that when the quadrupole transition rates follow rotational systematics, the excitation energy spectrum can still be close to the vibrational limit, Ref. [36]. The coexistence of both prolate and oblate configurations in this example could be another reason for the distortion in the energy spectrum. Within the Elliot SU(3) model this possibility was investigated in Ref. [28]. A possible interpretation has been offered in this reference as a result of coupling of two $SU(3)$ irreducible representations.

4.1.2 Triaxiality

The onset of triaxiality is best noticed by the presence of new low-lying levels 2_2, 3_1, 4_2, and 5_1 (see Subsec. 3.2.1). The excitation energies are subject to the relations $E(2_1) + E(2_2) = E(3_1)$ and $4E(2_1) + E(2_2) = E(5_1)$. It is remarkable that for the QQ Hamiltonian there is a good agreement; $R_{2_1 3_1} + R_{2_2 3_1} = 1.005$, and $4R_{2_1 5_1} + R_{2_2 5_1} = 1.026$ for the $(19/2)^6$ model. Here $R_{JJ'}$ as in Eq. (3.29) denotes the ratio of excitation energies. The K quantum numbers are mixed in triaxial systems. In our work we examine the two low-lying $J = 2$ states that are mixed configurations of the $K = 0$ and $K = 2$ states. We use the angle Γ to express the level of the K-mixing. This angle is determined by the three reciprocal moments of inertia $A_i = 1/(2\mathcal{L}_i)$, $i = 1, 2, 3$ of the rotor Hamiltonian 3.7

$$\tan 2\Gamma = \frac{\sqrt{3}(A_1 - A_2)}{A_1 + A_2 - 2A_3}.$$

The relation between the quadrupole moment and the moments of inertia (or between the parameters Γ and γ) is model dependent. In the irrotational flow model Γ is defined as $\Gamma = \{\text{arccot}\,[3\cot(3\gamma)] - \gamma\}/2$, which gives $\Gamma \ll \gamma$ for small triaxiality; a rather different result emerges in the rigid rotor model. We treat Γ and γ as being independent. Following Ref. [37] one can view the relative transition strength $b(E2, 0_{gs} \to 2_1) + b(E2, 0_{gs} \to 2_2) = 1$ and $\frac{7}{2} b(2_1 \to 2_2) + q^2(2_1) = 1$ for the $J = 2$ two-state model as the Pythagorean theorem for amplitudes. The corresponding angles are related to the triaxiality and K-mixing angles as

$$\tan^2(\gamma - \Gamma) = \frac{B(E2, 0 \to 2_2)}{B(E2, 0 \to 2_1)}, \tag{4.1}$$

$$\tan^2(\gamma + 2\Gamma) = \frac{2B(2_1 \to 2_2)}{7\mathcal{Q}^2(2_1)}. \tag{4.2}$$

The triaxiality and K-mixing are small in the QQ Hamiltonian, see the discussion in Chapter 5. Correspondingly, these effects have a weak but detectable presence in the TBRE. For our studies of triaxiality in Fig. 4.4, we consider the $(19/2)^6$ model and select collective realizations with 0_{gs} and 2_1. In addition to that, we require that in the entire spectrum there is a 2_2 state with the quadrupole moment almost the same in magnitude but opposite in sign to that of the 2_1 state. We recall that for the triaxial rotor model $\mathcal{Q}(2_1) = -\mathcal{Q}(2_2)$ because the quadrupole tensor is traceless and in the space spanned by all possible J-states the sum of its diagonal elements is zero. We find that practically for all collective realizations, realizations with a strong transition between the 0_{gs} and 2_1 states ($b > 0.7$), which can be thought of as a $K = 0$ band, there is a second 2_2 state which is predominantly a $K = 2$ state. From the total number of random realizations, 18.3% are collective, and they have the second 2_2 state with the quadrupole moment opposite in sign and approximately, within 20%, equal to the quadrupole moment of the 2_1 state. We use the same shading

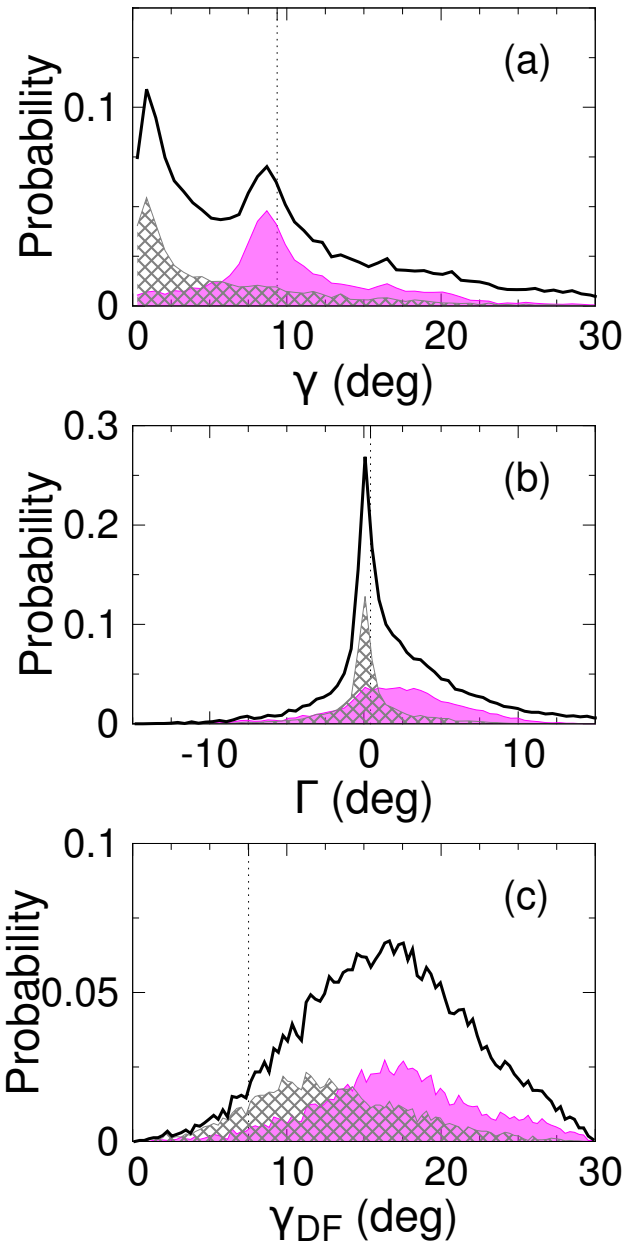

Figure 4.4: $(19/2)^6$. (a) The distribution of the triaxiality angle γ. (b) The distribution of the K-mixing angle Γ. (c) The distribution of the triaxiality angle γ_{DF} from the Davydov-Filippov model. The angles are obtained from Eqs. (4.1), (4.2) and (4.3). We select realizations with two states of spin 2 in the spectrum and require $b > 0.7$ and $q(2_1) \approx -q(2_2)$; 18.3% of realizations satisfy this set of restrictions. The realizations with prolate and oblate shapes are shaded with the same patterns as in Figs. 4.2 and 4.3. Vertical grid lines indicate the triaxiality parameters calculated from the QQ Hamiltonian, which are: $\gamma = 9.79°$, $\Gamma = 0.73°$, and $\gamma_{DF} = 7.52°$.

as in Fig. 4.3 to separate prolate and oblate shapes. In Figs. 4.4(a) and 4.4(b) we show the distributions of the triaxiality angle γ and K-mixing angle Γ, respectively (these angles are determined from Eqs. (4.1) and (4.2). The ratio of the excitation energies of the 2_1 and 2_2 states provides an additional independent way to evaluate the triaxiality. Shown in Fig. 4.4(c) is the distribution of the triaxiality angle γ_{DF} calculated using this ratio and assuming the Davydov-Filippov model of irrotational flow, as

$$\sin^2(3\gamma_{DF}) = \frac{9}{2}\frac{R_{2_1 2_2}}{(1+R_{2_1 2_2})^2}. \tag{4.3}$$

For small triaxiality $\gamma_{DF}^2 \approx 0.5 R_{2_1 2_2}$.

In the $(19/2)^6$ model one most commonly finds collective realizations with oblate intrinsic deformation and $s \approx 1$, and these realizations are triaxial with $\gamma \approx 9^\circ$, Fig. 4.4(a). This result is consistent with what is expected from the QQ Hamiltonian, see the summary in Tab. 5.2. The deformation parameters for the ground state band of the QQ Hamiltonian are indicated with vertical grid lines. The less frequent prolate cases are nearly axially symmetric. The ratio of the excitation energies $R_{2_2 2_1}$ used to obtain γ_{DF} in Fig. 4.4(c), appears to be lower in the TBRE than predictions of the Davydov-Filippov model for the peak value of γ (Fig. 4.4(a)). This finding is similar to the result shown in Fig. 4.3(b), where R_{42} is lower than expected for the rotor. As discussed above, we believe that the excitation energies are influenced significantly by non-collective features.

4.1.3 Higher multipole moments

It is known that in the TBRE the probability to find a 0_{gs} state followed by either one of the states $2_\mathbf{1}$, $4_\mathbf{1}$, $6_\mathbf{1}$, or $8_\mathbf{1}$ is disproportionally large as compared to what is statistically expected. For the $(19/2)^6$ model, the corresponding probabilities are 10.4%, 17.3%, 11.9% and 1.8% and, for the $(19/2)^8$ model, they are 7.47%, 7.99%, 16.87%, and 2.36%. In an attempt to detect collectivities of higher order, we repeat

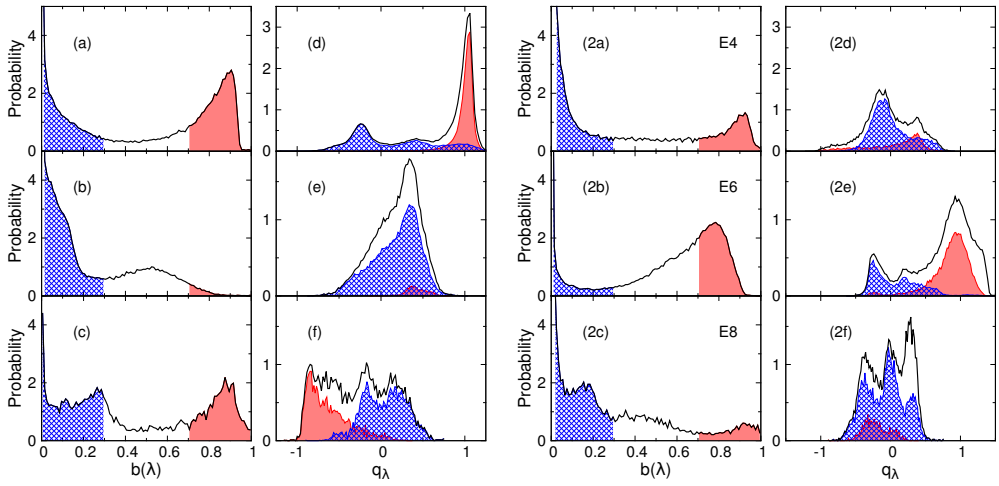

(1) $(19/2)^6$ (2) $(19/2)^8$

Figure 4.5: (a)-(c) The distributions of the fractional collectivity $b(\lambda)$ for three multipoles with $\lambda = 4$, 6 and 8 correspondingly; (d)-(f) the distribution of the intrinsic multipole moments q_λ for $\lambda = 4$, 6 and 8. Two single-level systems are considered: (1) $(19/2)^6$ and (2) $(19/2)^8$. Here we include realizations where in addition to 0_{gs} the first excited state is either $4_{\mathbf{1}}$, or $6_{\mathbf{1}}$, or $8_{\mathbf{1}}$. The shaded areas correspond to collective and non-collective modes with $b(\lambda) > 0.7$ and $b(\lambda) < 0.3$, respectively.

the previous study of collectivity, but target the collective realizations of multipolarity $\lambda = 4$, 6, and 8; we explore the fractional collectivity $b(\lambda) \equiv b(E\lambda, 0_{gs} \rightarrow \lambda_1)$ and the multipole moment $q_\lambda \equiv q_\lambda(\lambda_1)$, for realizations where spin of the first excited state is λ. As evident from Fig. 4.5, formation of the intrinsic shapes with deformations of multipolarities $\lambda = 4, 6$ and 8 is present in the TBRE. There is a sizable number of collective realizations, $b(\lambda) > 0.7$, with $\lambda = 4$ and 8 for $N = 6$ particles in the $j = 19/2$ orbital, and $\lambda = 4$ and 6 for $N = 8$ particles (shaded in red). The multipole moments have a specific sign for these samples. In contrast, the deformation with $\lambda = 6$ (8) does not develop in the system with $N = 6$ (8) : the realizations are mostly non-collective, $b(\lambda) < 0.7$ (shaded in blue), and the corresponding moment has a peak near zero. The observed multipole collectivities may be related to the symmetries discussed in Ref. [34].

4.1.4 Multipole structure of the Hamiltonian

In this subsection we discuss the multipole structure of a generic two-body Hamiltonian in the single j level model and its reflection in the TBRE regularities. For this purpose we use a larger system of 8 nucleons in the same model space with $j = 19/2$. The quadrupole collectivity summarized for this model in Figs. 4.6, 4.7 and 4.8 is similar to what was observed in the case of the $(19/2)^6$ model (Figs. 4.1, 4.2 and 4.3). The main difference is that only oblate ground state configurations are seen.

The collectivities observed in the single j studies are deeply rooted in the underlying geometric structure of the Hamiltonian. To pinpoint the multipole collectivities we write the two-body Hamiltonian (1.2) in the particle-hole channel

$$H^{(2)} = \sum_{\mathcal{K}} \tilde{V}_{\mathcal{K}} \sum_{k} \left(a_{jm_1} a^\dagger_{jm_2} \right)_{\mathcal{K}-k} \left(a^\dagger_{jm_1} a_{jm_2} \right)_{\mathcal{K}k}, \tag{4.4}$$

where a particle-hole operator $\left(a^\dagger_{jm_1} a_{jm_2} \right)_{\mathcal{K}k}$ represents the multipole operator (3.1) in the second-quantized form.

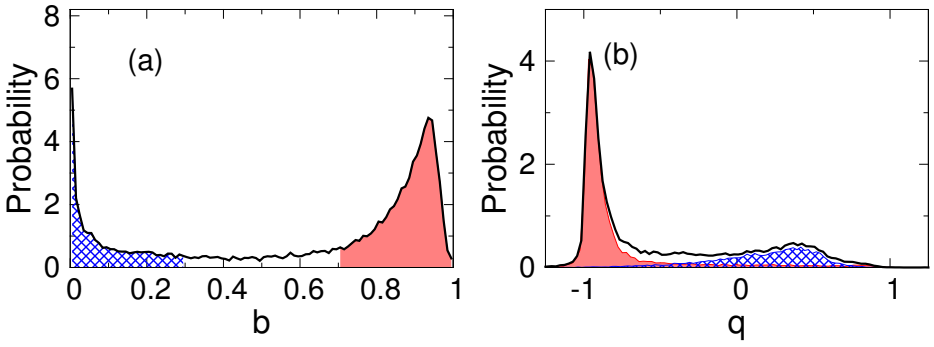

Figure 4.6: $(19/2)^8$. The same figure as Fig. 4.1 but for the 8-particle system. (a) The distribution of the fractional collectivity b. (b) The distribution of the intrinsic quadrupole moment q. The histogram is comprised of 7.5% of random spectra with 0_{gs} and 2_1 states. Shaded areas correspond to 4.6% of collective realizations ($b > 0.7$) and 1.9% of non-collective realizations ($b < 0.7$). This figure is analogous to Figs. 4.1 and 4.5, and the same shading is used in these figures.

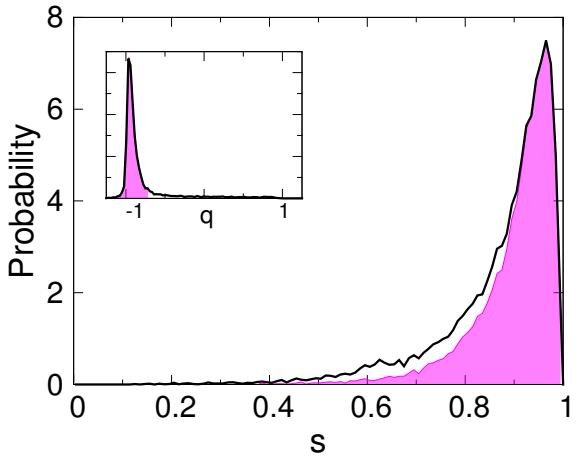

Figure 4.7: $(19/2)^8$. The same figure as Fig. 4.2 but for the 8-particle system. The distribution of the relative transition strength rule s for the collective realizations. This figure is analogous to Fig. 4.2, and the same shading is used as in Figs. 4.2 and 4.3, however only oblate shapes ($q < -0.7$) are seen.

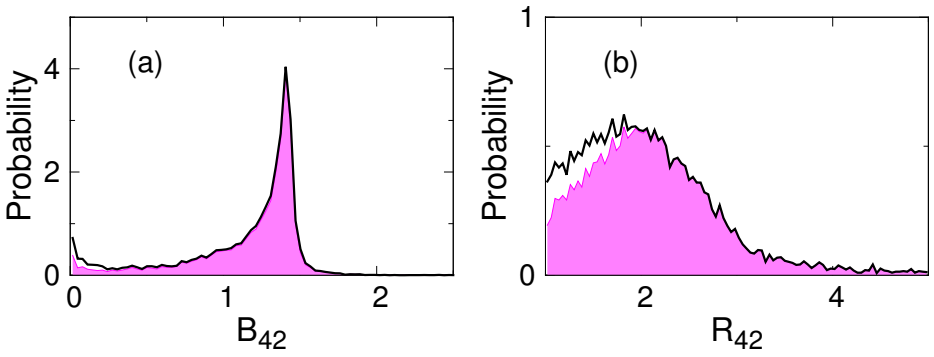

Figure 4.8: $(19/2)^8$. Same as Fig. 4.3 but for the 8-particle system. (a) The distribution of the deexcitation ratio B_{42}. (b) The distribution of the excitation energy ratio R_{42}.

The interaction parameters $\tilde{V}_\mathcal{K}$ in the particle-hole channel are determined from those in the particle-particle channel V_L via the Pandya transformation

$$\tilde{V}_\mathcal{K} = \sum_L (2L+1)\chi_L^\mathcal{K} V_L. \tag{4.5}$$

The transformation coefficients

$$\chi_L^\mathcal{K} = \left\{ \begin{array}{ccc} j & j & \mathcal{K} \\ j & j & L \end{array} \right\},$$

are six-j recoupling coefficients. On a single level only even values of the two-particle angular momenta L are allowed by the Fermi statistics, giving $j+1/2$ interaction parameters V_L. In studies of the TBRE a set of these parameters can be viewed as a random vector in the $j+1/2$ dimensional space.

There is no such restriction on the particle-hole angular momentum, thus the inverse transformation

$$V_L = \sum_\mathcal{K} (2\mathcal{K}+1)\chi_\mathcal{K}^L \tilde{V}_\mathcal{K} \tag{4.6}$$

may produce some unphysical V_L with odd values of L. Such Pauli-forbidden terms in the Hamiltonian do not generate any dynamics. Therefore, the $2j+1$ parameters $\tilde{V}_\mathcal{K}$ contain passive components, which can be removed making $\tilde{V}_\mathcal{K}$ linearly dependent [35].

The interaction terms that correspond to the multipoles with momentum $\mathcal{K} = 0$ and $\mathcal{K} = 1$ are constants of motion [38].

The $\mathcal{K} = 0$ term in (4.4) describes the nucleon-nucleon interaction, which is the same for all angular momentum channels, $V_L = \chi^0_L = \text{const}$, as follows from Eq. (4.6). The monopole Hamiltonian is proportional to the number of particle pairs in a system. It has no dynamical effect, nor any effect on the probability to observe a certain ground-state spin. Thus, one can constrain the TBRE by projecting out the monopole component χ^0_L as follows,

$$V_L \to V_L - \chi^0_L \frac{\sum_{L'}(2L'+1)\chi^0_{L'}\, V_{L'}}{\sum_{L'}(2L'+1)\left(\chi^0_{L'}\right)^2}. \tag{4.7}$$

This effectively reduces the number of independent parameters V_L.

For a single j model space, the $\mathcal{K} = 1$ multipole is proportional to the angular momentum operators $\mathcal{M}_{1\kappa} \sim J_\kappa$. Therefore the $\mathcal{K} = 1$ interaction leads to a rotational $E(J) \sim J(J+1)$ spectrum with $\tilde{V}_{\mathcal{K}=1}$ defining the moment of inertia. In the particle-particle channel the J^2 operator is obtained with $V_L = \chi^1_L \sim \text{const} + L(L+1)$. Inversely, those interactions that lead to positive $\mathcal{K} = 1$ in Eq. (4.5) are likely to result in the ground-state spin being zero [3]. The exact J^2 operator component in the interaction can be removed by orthogonalization to χ^1_L following Eq. (4.7).

We emphasize that the $\mathcal{K} = 0$ projection in Eq. (4.7) amounts to an energy shift for all states, which is irrelevant and so we do not discuss it. For $\mathcal{K} = 1$ the projected Hamiltonian is still dynamically identical to the original one; all eigenvectors remain unchanged, but the energies of states are modified in accordance with their spin. The changes are no longer trivial for the quadrupole term $\mathcal{K} = 2$, which corresponds to the QQ interaction discussed in Sec. 3.

The role of different multipoles in the TBRE is studied in Fig. 4.9 and 4.10, where we remove interaction components using the Graham-Schmidt projection procedure. The projection of the pairing interaction $V_L = \delta_{L,0}$ has been extensively discussed in

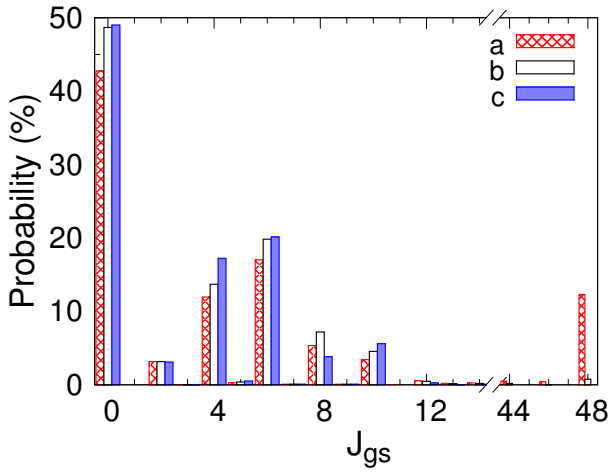

Figure 4.9: $(19/2)^8$. Ground-state spin statistics for three random ensembles: (a) the TBRE, (b) the TBRE without a J^2 term, and (c) the TBRE without both, J^2 and QQ terms.

Ref. [3]. Since the removal of pairing does not lead to any qualitative change we forgo this topic in what follows.

The probability to observe a certain ground-state spin for the $(19/2)^8$ system is shown in Fig. 4.9. Three cases of random ensembles are reviewed: (a) the traditional TBRE case where all $j+1/2$ interaction parameters V_L are random Gaussian variables; (b) the case where $\mathcal{K} = 1$ term is removed; and (c) the case where $\mathcal{K} = 1$ and 2 multipole components are removed from the Hamiltonian. While the wave functions in ensembles (a) and (b) are identical, the ground-state spin distributions are different. The determining role of the J^2 moment-of-inertia-like term has been discussed before; it appears to be fully responsible for the cases with the maximum possible spin [17]. As shown in Fig. 4.9, the states with the maximum spin almost never occur as ground states in ensembles (b) and (c), where the J^2 term is removed.

The ensembles (b) and (c) shown in Fig. 4.9 appears to have similar ground-state spin distributions but the behavior of the fractional collectivity is different. In Fig. 4.10 for all three ensembles we show the distribution of the fractional collectivity

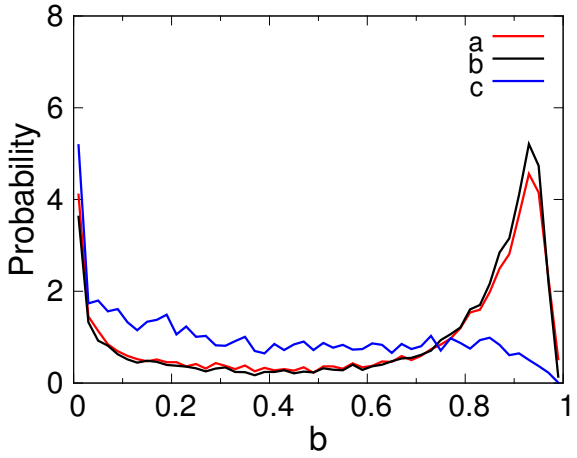

Figure 4.10: $(19/2)^8$. The distribution of the fractional collectivity b for the same three random ensembles as in Fig. 4.9. We select realizations with the ground state 0_{gs} followed by the first excited state $2_{\mathbf{1}}$. The fraction of such cases for ensembles (a), (b), and (c) is 7.6%, 8.2% and 4.7%, respectively.

in transition between the 0_{gs} and $2_{\mathbf{1}}$ states. The fraction of such cases for ensembles (a), (b), and (c) is 7.6%, 8.2%, and 4.7%, respectively. It is evident that this collectivity disappears once the quadrupole component in the interaction is removed. Thus, we conclude that the quadrupole-quadrupole component in the interaction generates deformations and is responsible for the rotational behavior observed.

4.2 Models beyond single j

In this section we expand the scope of our models and consider systems with two single-particle levels. The richer geometry allows one to study the effects of the particle-hole conjugation, different structures of the multipole operators, and the role of parity of single particle levels.

The first two-level model space we discuss has two degenerate levels $j_1 = j_2$ of the same parity. Because the levels have the same parity, the effective spherical Hartree-Fock mean-field Hamiltonian can contain terms of a mixed structure

such as $a^\dagger_{j_1} a_{j_2}$, and these terms are scalars for $j_1 = j_2$. There is also some flexibility in the choice of the single-particle matrix elements of the multipole operator $\mathcal{M}_{\lambda\mu}$, which depend on the radial overlap of the operator r^λ. We choose the radial overlap to be diagonal $\langle j_1|r^\lambda|j_1\rangle = \langle j_2|r^\lambda|j_2\rangle$ and $\langle j_1|r^\lambda|j_2\rangle = 0$; another possibility, with $\langle j_1|r^\lambda|j_1\rangle = \langle j_2|r^\lambda|j_2\rangle = \langle j_1|r^\lambda|j_2\rangle$, has been explored and led to no substantial difference. Shown in Figs. 4.11 are the distributions of the fractional collectivity and quadrupole moment for multipole operators with $\lambda = 2, 4, 6, 8$ in the $(13/2^+, 13/2^+)^6$ system, namely with 6 nucleons placed in two $j_1 = j_2 = 13/2$ orbitals. In the case of the $E2$ and $E4$ multipole operators, the corresponding moments have a definite type of deformation. The quadrupole moment has two peaks on the oblate side which are made up by collective realizations with $b > 0.7$ and a peak at zero attributed to non-collective realizations with $b < 0.3$. A similar picture is observed for the hexadecapole moment ($\lambda = 4$), with one collective peak on the positive side and non-collective peak around zero. For higher multipoles with $\lambda = 6$ and 8, the number of collective spectra falls drastically, resulting in a single peak around zero for the corresponding multipole moments.

A structurally different model is examined in Fig. 4.12, here two levels of equal spin and different parity are considered. The matrix elements of the Hamiltonian are now restricted by parity, which reduces the number of the two-body parameters (from 49 to 35 parameters for $N = 6$ particles in the $j_1 = j_2 = 13/2$ space). The same diagonal structure of the multipole operators with $\lambda = 2$ and 4 is used as in the $(13/2^+, 13/2^+)^6$ system. A model space of this kind has been explored in Ref. [39] because it is the simplest valence space that allows for collective quadrupole and octupole modes. (The prevalence of positive parity ground states is remarkable in this model [see Fig. 2.1(a)].) As compared with the $(13/2^+, 13/2^+)^6$ model, in the $(13/2^+, 13/2^-)^6$ model the fraction of collective realization is approximately the same. (For different-parity levels, the fraction of collective samples with $b(\lambda) > 0.7$ is 6.9%

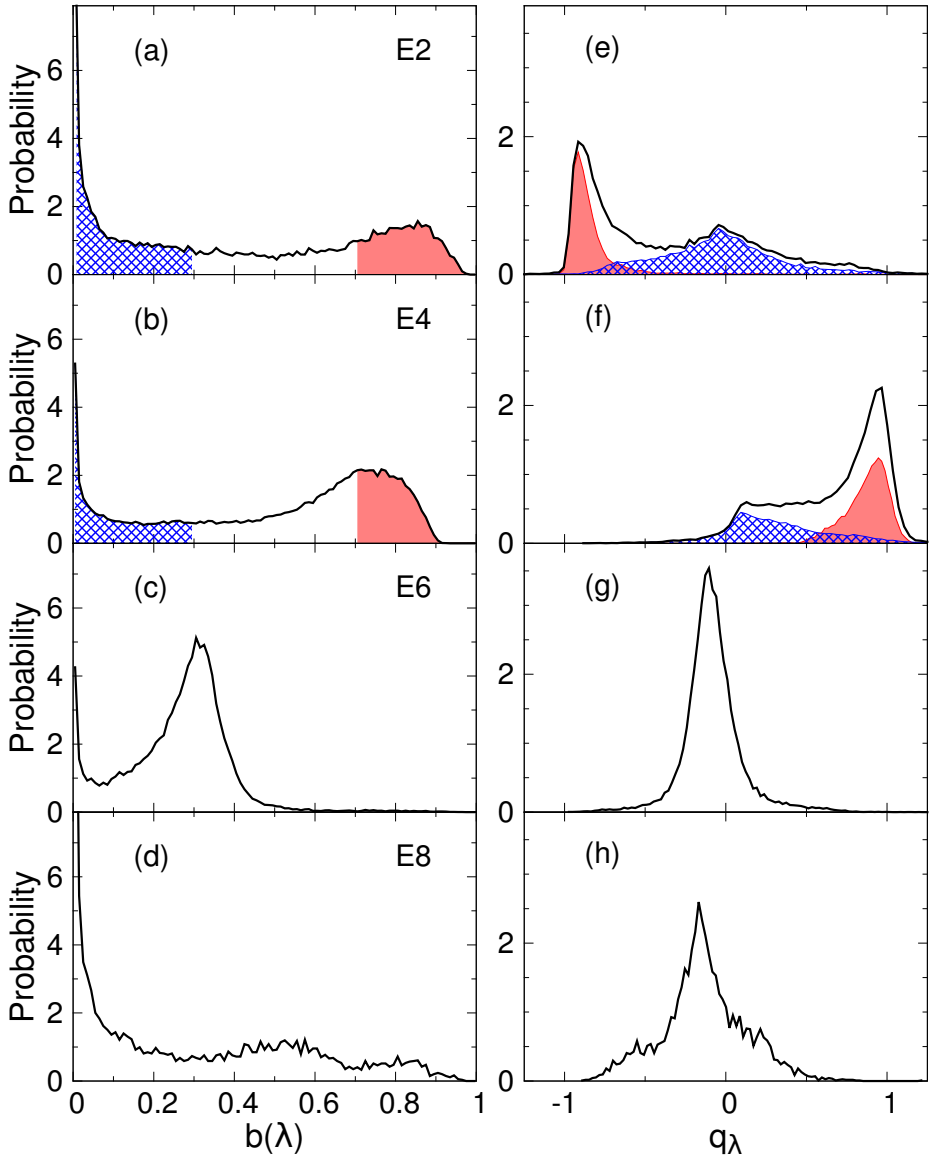

Figure 4.11: $(13/2^+, 13/2^+)^6$. (a)-(d) The distributions of the fractional collectivity $b(\lambda)$ for $\lambda = 2$, 4, 6, 8; (e)-(h) the distributions of the intrinsic multipole moments q_λ for multipoles with $\lambda = 2$, 4, 6, 8. The single-particle levels are degenerate. Shaded areas correspond to collective $b(\lambda) > 0.7$ and non-collective $b(\lambda) < 0.3$ modes. This figure is analogous to Figs. 4.1, 4.5, and 4.6, and the same shading is used in these figures.

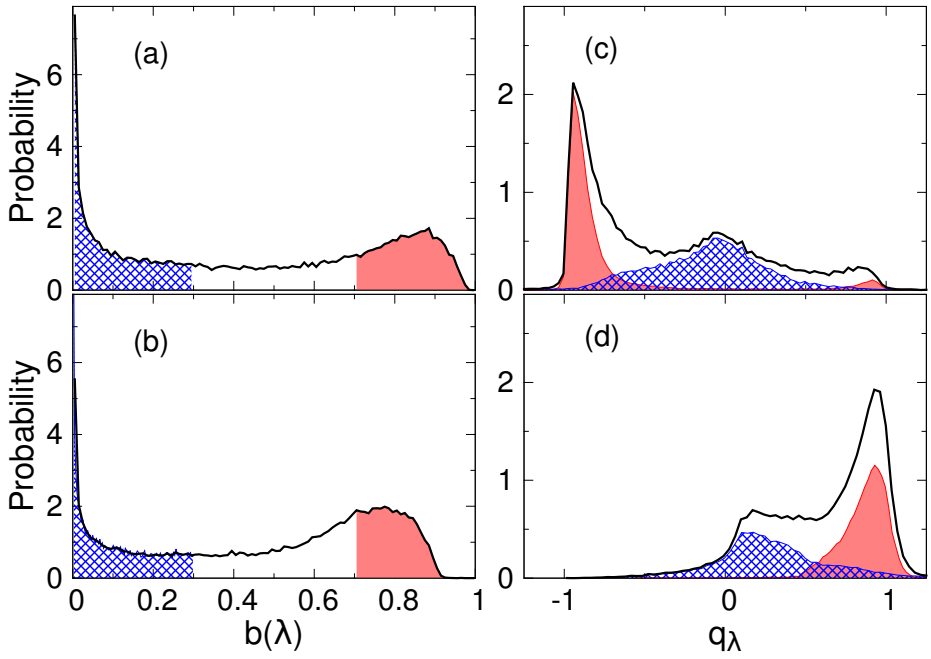

Figure 4.12: $(13/2^+, 13/2^-)^6$. (a) The distributions of the fractional collectivity for the quadrupole transition; (b) the distributions of the fractional collectivity for the hexadecapole ($\lambda = 4$) transition; (c) the distribution of the quadrupole moment; (d) the distribution of the hexadecapole moment. The shading is the same as in Figs. 4.1, 4.5, 4.6, and 4.11.

(13.7%) for $\lambda = 2$ ($\lambda = 4$) from the total number of realizations against 4.1% (13.6%) for the same-parity levels.) The distribution of the multipole moments is also not affected by the parity of the single-particle levels.

In general, results for the quadrupole and hexadecapole collectivities, see Figs. 4.11 and 4.12, are very similar to those observed in the single j level models (Figs. 4.1, 4.5, and 4.6). The major features in the distributions of b and q persist despite a larger number of random parameters, the more complex geometry of the model, and, as a result, more chaotic dynamics on two levels. In all instances there is a peak in the distribution of the fractional collectivity b near 1, indicating a sizable number of collective cases. The quadrupole moment for collective states has a well-defined

peak on the oblate side. The non-collective realizations, $b < 0.3$, appear to have quadrupole moment distribution centered at zero (shaded in blue).

For systems with exact particle-hole symmetry the quadrupole moment for particles is equal in magnitude and opposite in sign to that of holes. Moreover, properties such as excitation energies, the spins of states, and transition rates, are exactly equal for particle-hole conjugated systems. The particle-to-hole transformation for any two-body Hamiltonian amounts to the same Hamiltonian for holes but with an additional one-body term (the single-particle energies) [35], thus the symmetry is not exact for the $(13/2, 13/2)$ model space. Nevertheless for holes in the TBRE, a random ensemble with two-body matrix elements selected symmetrically about zero, the one-body term averages to zero leading to nearly symmetric results. This is confirmed in Figs. 4.13 and 4.11; the distribution of the quadrupole moment for a system with 6 holes looks the same as that of 6 particles, reflected around zero. The only difference is that the Hamiltonian for holes contains random single-particle energies, which leads to a different number of collective realizations. For a system with 6 holes, or $N = 22$ particles, the fractions of realizations with the spin 0, 2 and 0, 4 lowest sequences are larger than for its particle-hole conjugated system, and there are more collective realizations for the $(19/2,\ 19/2)^{22}$ system than for $(19/2,\ 19/2)^{6}$ (see Tab. 4.1).

4.3 Realistic model space

The schematic models discussed in the previous sections appear to have collective deformation and possess a rotational low-lying spectrum. However, to what extent they reflect the dynamics of realistic nuclei remains a question. The sign of the deformation seems to be inconsistent with the prolate dominance (a detailed discussion of the prolate dominance is given in Ch. 5), moreover semi-magic nuclei (nuclei with only one type of valence nucleons) are generally not deformed. To address these issues we examine a more realistic model space consisting of the $0f_{7/2}$ and $1p_{3/2}$ single-particle

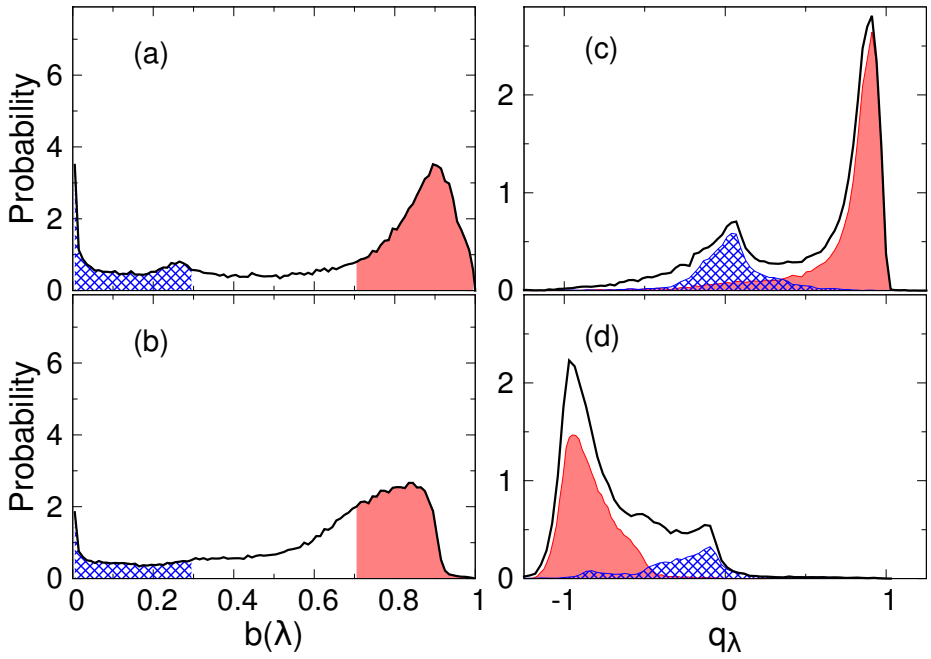

Figure 4.13: $(13/2^+, 13/2^+)^{22}$. (a) The distributions of the fractional collectivity for the quadrupole transition; (b) the distributions of the fractional collectivity for the hexadecapole ($\lambda = 4$) transition; (c) the distribution of the quadrupole moment; (d) the distribution of the hexadecapole moment. This system is particle-hole conjugated relative to that in Fig. 4.11. The shading is the same as in Figs. 4.1, 4.5, 4.6, 4.11 and 4.12.

Table 4.1: Comparison of the fraction of the $E2$ and $E4$ collective spectra for the $(13/2^+, 13/2^+)^6$ system and its particle-hole conjugated system $(13/2^+, 13/2^+)^{22}$. Given are the percentage of the realizations with the 0,2 and 0,4 sequence n$(0, 2)$ and n$(0, 4)$ and the percentage of the collective realizations n$(b > 0.7)$ and n$(b(4) > 0.7)$. The total number of realizations is 500,000 for both systems.

	$N = 6$	$N = 22$
n$(0, 2)$	4.1	8.1
n$(b > 0.7)$	1.2	4.8
n$(0, 4)$	13.6	20.5
n$(b(4) > 0.7)$	4.5	10.2

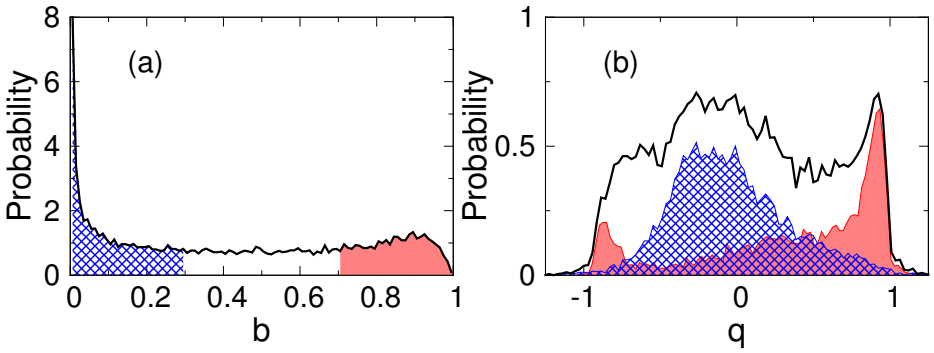

Figure 4.14: $(0f_{7/2}, 1p_{3/2})^8$. (a) The distribution of the fractional collectivity b. (b) The distribution of the intrinsic quadrupole moment q. The solid black line outlines the probability distribution for the 31% of realizations with the 0_{gs} state followed by the 2_1 first excited state, both states with isospin $T = 0$. Here 8.8% of realizations are collective and 12.8% are non-collective.

levels, allowing both protons and neutrons. For this model we consider harmonic oscillator wave functions for the calculations of the matrix element of the quadrupole operator; we use the same effective charge for both types of nucleons. The multipole operator in this form facilitates the comparison with the SU(3) group.

In Fig. 4.14 we present our results for a system with 8 nucleons, 4 protons and 4 neutrons. This corresponds to the configuration space of the ^{48}Cr nucleus. In Fig. 4.14(a), where the fractional collectivity b is shown, the peak that corresponds to collective realizations is observed. The distribution of the quadrupole moment shows prolate and oblate peaks, see Fig. 4.14(b); these peaks are especially clear for collective realizations. Non-collective cases appear to center around $q = 0$ (shaded in blue). In agreement with the results in Ref. [40], the prolate peak is larger, showing the prolate dominance.

In Fig. 4.15 we focus on the 8.8% of realizations that are collective. The quadrupole moments in Fig. 4.14(b) are further separated into prolate $q > 0.7$ and oblate $q < -0.7$ cases as shown in the inset in Fig. 4.15. The same shading is used in the main figure, showing the distribution of the reduced quadrupole strength s. The maximum

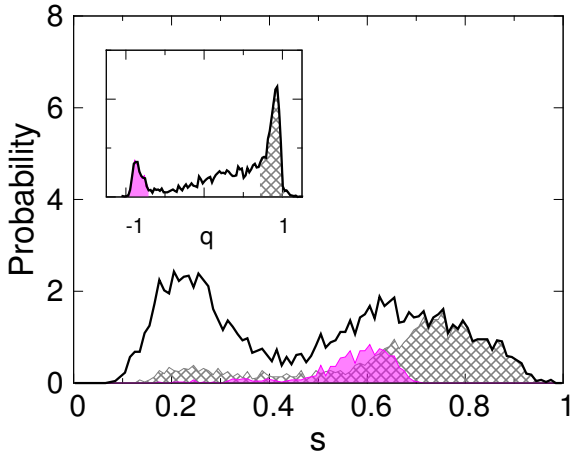

Figure 4.15: $(0f_{7/2}, 1p_{3/2})^8$. The distribution of the relative transition strength s for the collective realizations (shaded in Fig. 4.14). The 3.6% of prolate cases and 1.0% of oblate are identified with shades of color and pattern (see the inset).

possible value $s = 1$ is reached when the ground state wave function of the randomly selected Hamiltonian coincides with that of the QQ Hamiltonian. The $J = 0$, $T = 0$ ground state of the QQ Hamiltonian with $s = 1$ posses a prolate deformation in this valence space. The oblate shapes appear to peak around $s = 0.6$.

The distributions of the ratios B_{42} and R_{42} for collective realizations are shown in Fig. 4.16. This figure can be compared to Fig. 4.3; we use the same shading in both figures to separate the prolate and oblate collective cases. In contrast to Fig. 4.3(a), both prolate and oblate realizations in Fig. 4.16(a) have band structure with deexcitation ratio B_{42} that is consistent with the rotational value. This ensemble, based on a more realistic model space, appears to have an energy spectrum that is closer to rotational; the distribution of R_{42} in Fig. 4.16(b) is broad, but it has a peak around the rotor value of 10/3. The collectivities observed in the two-body random ensembles are influenced by the single-particle level structure which could be interpreted as a representation of the mean-field structure of the core. In many cases the presence of the shell structure inhibits the role of the two-body Hamiltonian resulting in re-

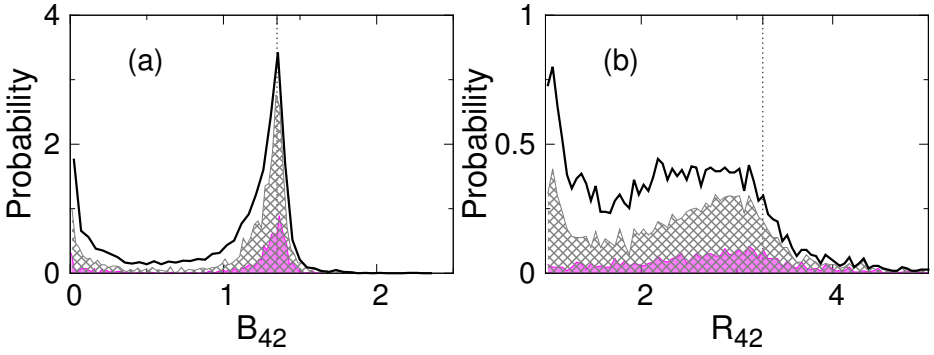

Figure 4.16: $(0f_{7/2}, 1p_{3/2})^8$. (a) The distribution of the deexcitation ratio B_{42} defined in Eq. (3.30). (b) The distribution of the excitation energy ratio R_{42} defined in Eq. (3.29). Collective realization discussed in Fig. 4.14 are selected and, in addition, we require that the second excited state has spin 4. The fraction of such cases is 4.2%, with 2.4% being prolate and 0.6% being oblate, they are shaded separately with the same patterns as in Fig. 4.15. The values for B_{42} and R_{42} from the QQ Hamiltonian listed in Tab. 5.1 are shown with the vertical grid lines. This figure is analogous to Fig. 4.3, and the same shading is used as in Figs. 4.2-4.4 and 4.15.

duced collectivity. This effect is known in realistic nuclei and is seen in model studies including SU(3) and seniority models for deformation and pairing. In Fig. 4.17 we demonstrate the effect of the core's mean-filed by considering a situation with the following splitting of the single-particle energies $\delta\epsilon = \epsilon_{p3/2} - \epsilon_{f7/2} = 7$. The unit of energy is determined by the variance of the two-body matrix elements, which can also be expressed in terms of the variance of the level spectrum for the two-particle system. The chance to observe the 0_{gs},$2_{\mathbf{1}}$ sequence in this case is 15.7%, which is half of that in the degenerate model. Among these realizations there is a noticeable number of collective (2.9% of the total number) and non-collective (8.1% of the total number) realizations. The distributions of the fractional collectivity and the quadrupole moment for theses realizations are shown in Fig. 4.17. Another difference between degenerate and non-degenerate systems is a presence of only prolate deformation in the non-degenerate system, see Fig. 4.18. However, the overall manifestations of collectivity are similar to those of the degenerate model.

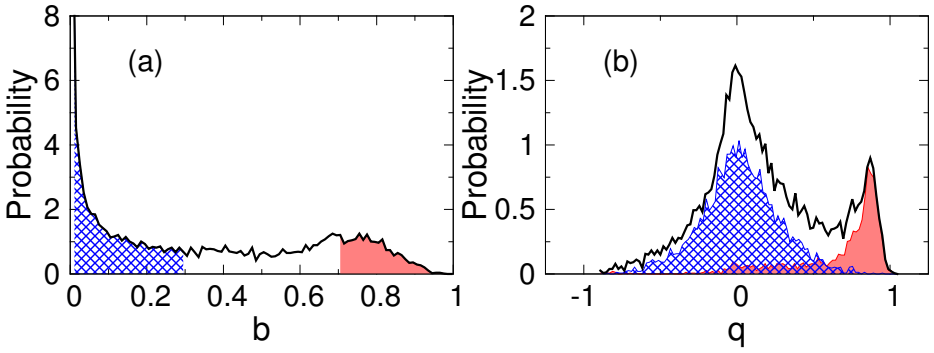

Figure 4.17: $(0f_{7/2}, 1p_{3/2})^8, \delta\epsilon = 7$. (a) The distribution of the fractional collectivity b; (b) the distribution of the intrinsic quadrupole moment q. The system is non-degenerate with single-particle energies $\epsilon(f_{7/2}) = 0$ and $\epsilon(p_{3/2}) = 7$ and $\delta\epsilon = \epsilon(p_{3/2}) - \epsilon(f_{7/2})$. The solid black line outlines the probability distribution for the 15.7% of realizations with the 0_{gs} state followed by the 2_1 first excited state, both states with isospin $T = 0$. Here 2.9% of realizations are collective and 8.1% are non-collective.

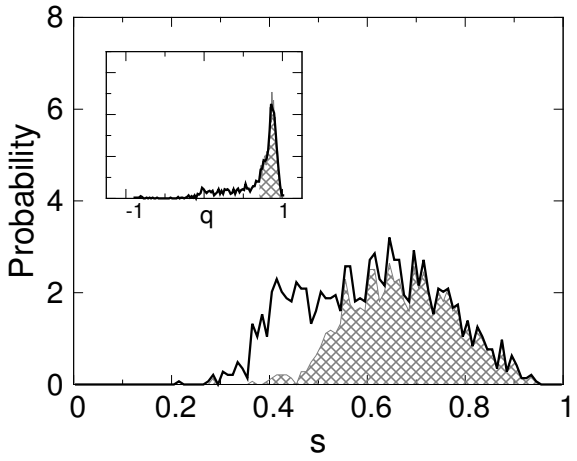

Figure 4.18: $(0f_{7/2}, 1p_{3/2})^8, \delta\epsilon = 7$. The distribution of the relative transition strength s for the collective realizations (shaded in red in Fig. 4.17). The system is non-degenerate with single-particle energies $\epsilon(f_{7/2}) = 0$ and $\epsilon(p_{3/2}) = 7$ and $\delta\epsilon = \epsilon(p_{3/2}) - \epsilon(f_{7/2})$. The 1.9% of prolate cases are identified with a pattern shade (see the inset).

As concluded in Ref. [40], collective realizations appear to correspond to correlated interaction matrix elements. Similarly to the single j level model (Fig. 4.10), it is natural to attribute this to the QQ component in the Hamiltonian. We examine the distribution of overlaps x between the ground state wave functions of the two-body random ensemble $|0_{gs}(\mathrm{TBRE})\rangle$ and a ground state wave function of the QQ Hamiltonian

$$x = |\langle 0_{gs}(\mathrm{TBRE})|0_{gs}(\mathrm{QQ})\rangle|^2.$$

We select the 56.3% of realizations where the ground state quantum numbers are $J = 0$ and $T = 0$ (the ground state of the QQ Hamiltonian has the same spin and isospin, $T = 0$ and $J = 0$). A similar approach has been used in investigations of pairing coherence in random ensembles [3]. The distribution for x shown in Fig. 4.19 is compared with the Porter-Thomas χ^2 distribution and with the overlap for pairing. The latter emerges for uncorrelated wave functions in the 126-dimensional space spanned by the $J = 0, T = 0$ wave functions. As shown in Fig. 4.19 the Porter-Thomas distribution drops abruptly, thus predicting that cases with large x are extremely unlikely. According to the Porter-Thomas distribution the probability to find $x > 0.1$ is only 0.03%, whereas in the TBRE, $x > 0.1$ in 18.8% of random realizations. As compared with the Porter-Thomas distribution, the pairing component of the interaction is also enhanced, although the overlap between wave-functions in the pairing and QQ Hamiltonians is not significant (11%). To emphasize the relation between the fractional collectivity b and the large QQ component in the wave function, we show in Fig. 4.19 the histogram for collective realizations with 0_{gs}, $2_{\mathbf{1}}$, and $b > 0.7$. It is clear that the collective transitions and rotational structure emerge when the component that corresponds to the eigenstate of the QQ Hamiltonian is large.

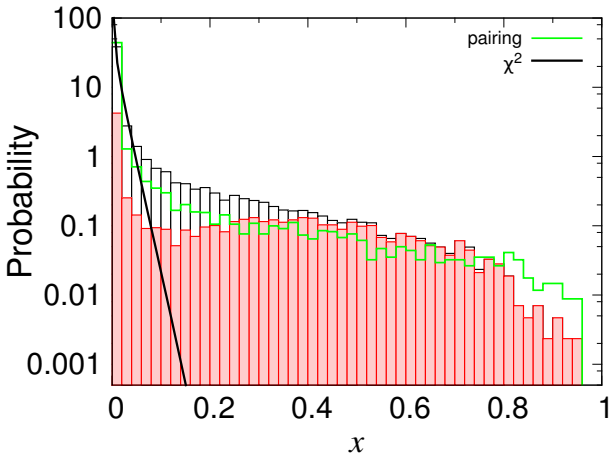

Figure 4.19: $(0f_{7/2}, 1p_{3/2})^8$. The distribution of the overlaps between the TBRE and QQ ground state wave functions. The results for all $J_{gs} = 0, T_{gs} = 0$ states are unshaded; the fraction of such realizations is 56.3%. Collective realizations that have $J = 2, T = 0$ as a first excited state and $b > 0.7$ are shaded (their fraction is 8.8%). The solid line shows the Porter-Thomas distribution, which is expected for the overlap between uncorrelated states.

CHAPTER 5

QQ HAMILTONIAN

5.1 Rotational bands

As we showed in the previous chapter, the QQ component in the random two-body Hamiltonians is a necessary ingredient for the emergence of quadrupole collectivity in the TBRE. It is also an important part of realistic shell-model potentials. In many respects, the QQ interaction and the geometry of the valence space determine formation of the rotational modes and their characteristics. Thus, in this chapter we address questions of the rotational systematics in the QQ Hamiltonian. We explore the impact of the model-space structure on rotational modes and, particularly, on shapes of deformation. Particle-hole symmetry is another factor that affects shapes of deformation, and its role is also investigated in this chapter. The QQ interaction is related to the Casimir operator of the Elliot SU(3) group (see Ch. 3). The SU(3) group is not exact in general. Where applicable, we compare our results for the QQ interaction with those of the exact SU(3) symmetry.

Table 5.1 includes spectral characteristics of the QQ Hamiltonian for a single orbital with $j = 19/2$, two-level models with $j_1 = j_2 = 13/2$ of the same and of opposite parity, and the realistic model spaces $0f_{7/2}, 1p_{3/2}$ and $0f_{5/2}, 0g_{9/2}$. Isospin is included in the latter two spaces, and the number of particles N refers to the sum of the number of protons and neutrons. Most of these model spaces are used in our study of collectivity in the TBRE in Ch. 4. The choice of systems is such that it allows one

to investigate various aspects that affect the spectrum of the QQ Hamiltonian, such as the geometry of the space, particle-hole symmetry, and the effects of isospin. The spectra for all systems have a ground state with spin zero and the first excited state with spin 2. The 2_1 state is connected with the 0_{gs} state by a strong $E2$ transition, this follows from the fact that values of the fractional collectivity b (Eq. 3.3) are close to 1. The values of the intrinsic quadrupole moment $q(2_1)$ are close to the axial-rotor value of 1 for all systems, except for those with half-filled shells ($N = 12$ in the $0f_{7/2}, 1p_{3/2}$ space). The deexcitation ratio B_{42} is consistent with the axial rotor value of $B_{42} \approx 1.43$ (from Eq. 3.25) with the exception of the $(0f_{7/2}, 1p_{3/2})^{10}$ systems with $\delta\epsilon \equiv \epsilon_{p_{3/2}} - \epsilon_{f_{7/2}} = 0, \pm 0.6$. The evidence of rotational structure in the QQ spectrum is further supported by the behaviour of the excitation energies. In the rigid-top limit $E(J) \propto J(J+1)$, and the excitation energy ratio is $R_{42} \approx 3.33$; for all systems R_{42} is close to this rigid-rotor value. Systems with an odd number of protons and neutrons ($N = 10$ in the $0f_{7/2}, 1p_{3/2}$ space) have isospin $T = 1$ in the ground state, and the states 2_1 and 2_2 are chosen of the same isospin as in the ground state.

An interesting question for deformed systems is the sign of the quadrupole moment. On a single level with one kind of nucleons, the shape of deformation is oblate (pancake-like) for shell occupancies less than a half. The particle-hole symmetry appears to be exact in this case, leading to the quadrupole moment of the same magnitude and opposite sign for particle-hole conjugated systems (not shown). An oblate shape of deformation at the beginning of the shell is also predicted for two two-level models with $j_1 = j_2 = 13/2$. In all instances of the realistic model space $(0f_{7/2}, 1p_{3/2})$, the deformation is prolate (cigar-like) at the beginning of the shell. For these model spaces, the same sign of deformation was observed in the TBRE for the majority of collective samples. If single-particle levels have opposite parity as in the $(0f_{5/2}, 0g_{9/2})$ model, the shape of deformation is oblate at the beginning of the shell. The statistics of the quadrupole moment in random ensembles for this system in Ref. [40] is

consistent with this observation for the QQ Hamiltonian.

The single-particle energies affects collective features. For example, in our study of the TBRE the presence of the core's structure reduces collectivity and affects its characteristics. As one can see comparing the degenerate case of the $(0f_{7/2}, 1p_{3/2})$ model, $\delta\epsilon = \epsilon_{p_{3/2}} - \epsilon_{f_{7/2}} = 0$, and non-degenerate cases with $\delta\epsilon = \pm 0.6, 4.2$ in Tab. 5.1, the collective observables are not sensitive to the structure of the single-particle levels. Also the dependence of the QQ spectrum on the shape of the single-particle potential is investigated for the $0f_{7/2}, 1p_{3/2}$ model, with the normal ordering of levels, when the $0f_{7/2}$ level lies lower than the $1p_{3/2}$ level, $\delta\epsilon = 0.6, 4.2$, and the inverse ordering, $\delta\epsilon = -0.6$. The position of the single-particle levels does not seem to affect the collective observables, except for the half-filled system, $N = 12$. A small deformation arises in the middle of the shell for non-degenerate levels, and its sign depends on the relative position of the single-particle levels.

Most of the systems discussed in Tab. 5.1 are triaxially deformed, which is pointed by the presence of the second state with spin 2, a typical signature of triaxiality. In the rigid-rotor triaxial model the dimension of the space with spin 2 is 2×2. Because the quadrupole tensor is traceless, the sum of the moments of two $J = 2$ states is equal to zero. Four cases studied in random ensembles and presented in Tab. 5.2 are triaxial. The values of the triaxiality angles γ, Γ, and γ_{DF} described in the two-band prescription in Ch. 3 are listed in Tab. 5.2, as well as the sums of excitation energy ratios: $R_{2_1 3_1} + R_{2_2 3_1}$ and $4R_{2_1 5_1} + R_{2_2 5_1}$ which are equal to 1 for a triaxial rotor [22]. The formation of triaxial mean field in the TBRE was investigated for the $(19/2)^6$ model, see Fig. 4.4. Values of the triaxiality angle γ and K-mixing angle Γ in the TBRE are in good agreement with the QQ values.

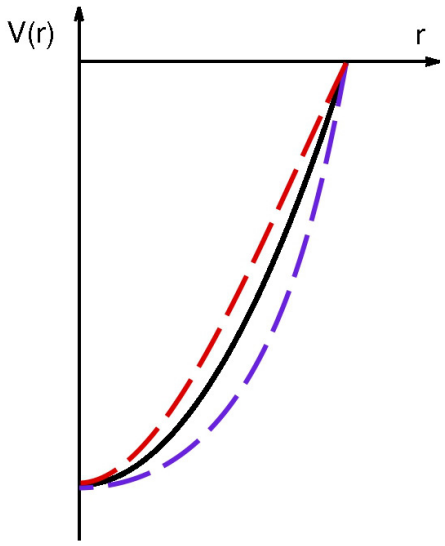

Figure 5.1: Shapes of the single-particle potential. The harmonic oscillator potential is shown with the black solid line. A steeper potential is shown with the red dashed line. The blue dashed line represents a flatter potential.

5.2 Shapes of deformation

Practically all deformed nuclei in nature are known to have a prolate shape in the ground state. This prolate dominance has been widely discussed in the literature [41, 42, 43, 44]. An effort to pinpoint the origin of the phenomenon using ensembles with random two-body interactions is presented in Ref. [40]. The role of the single-particle level structure in the prolate dominance is discussed by Hamamoto in Ref. [44]. In this chapter we explore the sign of deformation in the QQ Hamiltonian for particle-hole conjugated systems as the single-particle structure of the space varies.

The shape of the single-particle potential also affects the shape of deformation. The effect of both particle-hole symmetry and of the shape of the single-particle potential on the sign of deformation in the QQ Hamiltonian is studied for two model spaces.

The first model contains N protons and neutrons ($T_z = 0$) in the $(0_{f7/2}, 1p_{3/2})$

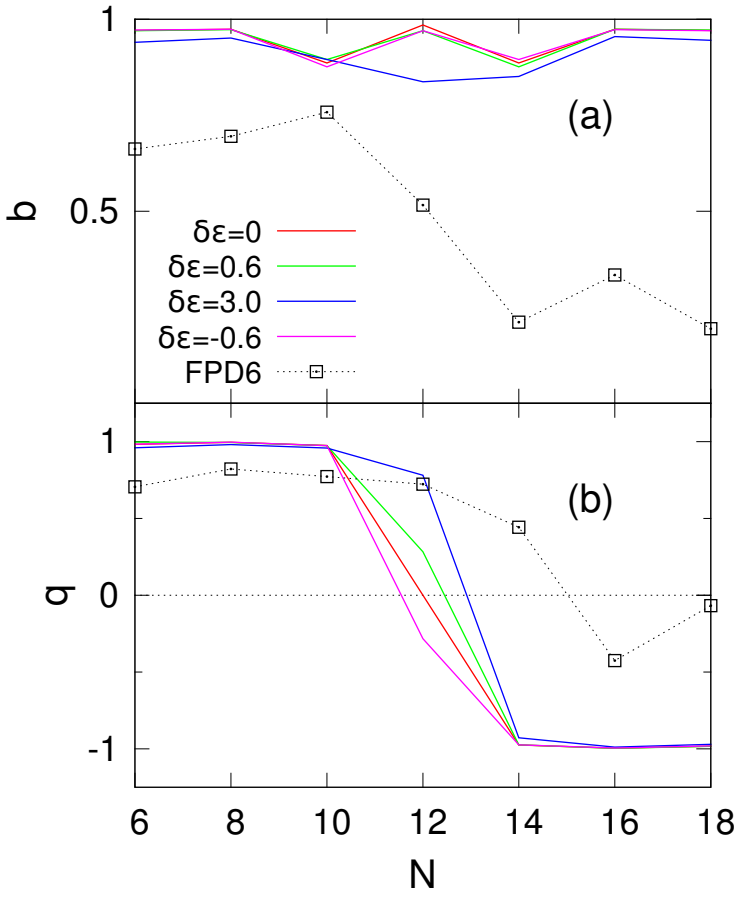

Figure 5.2: $(0f_{7/2}, 1p_{3/2})^N$. (a) The fractional collectivity and (b) the quadrupole moment of the 2_1 state for the QQ Hamiltonian. Four cases of the single-particle splitting $\delta\epsilon = \epsilon(1p_{3/2}) - \epsilon(0f_{7/2})$ are considered: $\delta\epsilon = 0, \pm 0.6, 3.0$. Predictions of the realistic FPD6 potential are shown with a dotted line with squares.

space. Some of the data for this space are listed in Tab. 5.1. Configurations of N particles in this valence space correspond to the shell configurations of ^{46}V, ^{48}Cr, ^{50}Mn, ^{52}Fe, ^{54}Co, ^{56}Ni, and ^{58}Cu for $N = 6, 8, 10, 12, 14, 16$, and 18, correspondingly. As mentioned earlier and seen from Fig. 5.2, the QQ Hamiltonian predicts prolate shape at the beginning of the shell for this system. As a further investigation of deformation shapes, we lift the degeneracy of the single-particle levels by $\delta\epsilon = \epsilon(1p_{3/2}) - \epsilon(0_{f7/2})$. Placing the $0f_{7/2}$ orbital lower than the $1p_{3/2}$ orbital corresponds to a flattening of the harmonic oscillator potential as shown with the blue line in Fig. 5.1. In the Nilsson potential this effect is simulated by introducing the l^2 term. For the reverse order of orbits, $1p_{3/2}, 0f_{7/2}$, the potential is steeper than the harmonic oscillator potential, and this is shown with the blue line in Fig. 5.1. Although the particle-hole symmetry is violated by single-particle level splitting, this does not affect the shape of deformation at the beginning and at the end of the shell. Less than half-filled and more than half-filled systems preserve their sign of deformation as compared with the degenerate case. A predominance of a certain deformation develops in the half-occupied shell, $N = 12$. For the half-filled non-degenerate systems, the shape of the mean field is defined by the relative capacity of the levels. Systems with the lower level of bigger capacity, that is bigger l, have a prolate shape, and vice versa. This is in agreement with the mean-field surface effect explored by Hamamoto and Mottelson [44]. It has been shown in this reference that for two deformed potentials, a harmonic oscillator potential and an infinite-well potential, a prolate shape is dominant for the one with a sharper surface, namely for the infinite well potential.

Results for the realistic shell-model potential FPD6 [45] are also shown in Fig. 5.2. According to these calculations, the deformation in the middle of the shell is indeed prolate. However in the systems at the end of the shell (N=14,16, and 18) with the realistic potential, the $0_{gs} \rightarrow 2_1$ transition is not very strong; b is only of order 20-30%. The value of the quadrupole moment $q \equiv q(2_1)$ for these systems points to

the noticeable violation of the particle-hole symmetry.

We performed a similar study for the complete *sd*-shell containing N nucleons. For this system we included the spin-orbit splitting which changes the energy of the single particle levels according to $\epsilon(d_{5/2}) = -kl/2$ and $\epsilon(d_{3/2}) = k(l+1)/2$, where k is a variable parameter. The largest dimension of the many-body space is 142 for the half-occupied system, $N = 6$, such a small dimensionality allowed us to perform an exact diagonalization for all N. Shown in Fig. 5.3 is the fractional collectivity of the ground state b and the quadrupole moment of the 2_1 state q for five strengths of the spin-orbit splitting k. What unifies all of these systems is the presence of two deformed states with spin 2 in the low-lying spectrum with the opposite sign of the quadrupole moment, which is a signature of triaxiality. However the behavior of these two states as a function of the spin-orbit splitting is quite different in systems with different N. For the $N = 4$ system the states are degenerate in the absence of the spin-orbit interaction. Once the degeneracy is removed, the states stay quite close in energy and their quadrupole moments are of nearly the same magnitude. In the half-filled shell, $N = 6$, the signature of the low-lying spectrum is a spin sequence 0,0,2,2. The two $J = 0$ states are almost degenerate, and so are the $J = 2$ states. The single-particle splitting resolves into two bands with each of the $J = 0$ state being a bandhead. The shape of the deformation of the lowest $J = 2$ state is oblate. A quite interesting behaviour is observed in the $N = 8$ system; this is the only system with the quadruple moment changing a sign as spin-orbit splitting increases. For comparison, the results of the shell model calculations with the realistic USD potential [46] are also shown in Fig. 5.3. According to the shell structure, these systems correspond to neutron-rich oxygen isotopes with tn excess of neutrons equal to N. The values of b and q for $k = 2$ follow the USD predictions most closely. On a side note, pairing and the intruder states play an important role in nuclei with a large excess of neutrons, and limitations to the QQ Hamiltonian in the *sd*-shell might not represent the realistic

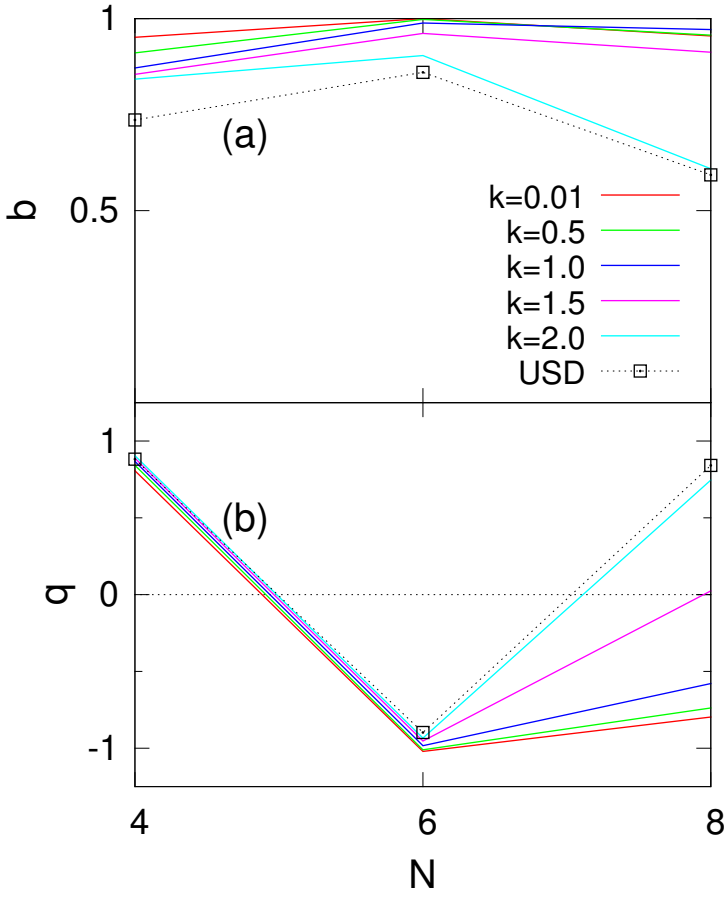

Figure 5.3: (a) The fractional collectivity and (b) the quadrupole moment of the 2_1 state for the QQ Hamiltonian for N particles in the *sd*-shell. Data is collected for five spin-orbit strengths k and the realistic shell model potential (USD).

picture.

To conclude this chapter we investigate the presence of the QQ component and the survival of the SU(3) structure in the ground state band in the realistic USD potential. For two configurations $(1s_{1/2}, 0d_{5/2}, 0d_{3/2})^4$ and $(1s_{1/2}, 0d_{5/2}, 0d_{3/2})^8$, which correspond to the shell-model configurations of the ^{20}O and ^{24}O nuclei and discussed in Fig. 5.3, we calculate overlaps between the ground state of the SU(3) group and the ground states of the QQ and USD potentials:

$$\begin{gathered} x(\mathrm{QQ}|\mathrm{SU(3)}) = |\langle 0_{gs}(\mathrm{QQ})|0_{gs}(\mathrm{SU(3)})\rangle|^2, \\ x(\mathrm{QQ}|\mathrm{USD}) = |\langle 0_{gs}(\mathrm{QQ})|0_{gs}(\mathrm{USD})\rangle|^2, \\ \text{and} \\ x(\mathrm{SU(3)}|\mathrm{USD}) = |\langle 0_{gs}(\mathrm{SU(3)})|0_{gs}(\mathrm{USD})\rangle|^2. \end{gathered} \tag{5.1}$$

In the case of these configurations, the sole difference between the interaction in the SU(3) model and in the QQ Hamiltonian is in the single-particle energies, which are non-degenerate in the latter model. These overlaps are listed in Tab. 5.3. For the ^{20}O configuration the large value of the overlap $x(\mathrm{QQ}|\mathrm{USD}) \sim 0.9$ points to close similarity in the ground-state structure in the QQ Hamiltonian and in the USD potential. This overlap is smaller for the ^{24}O configuration, ~ 0.4, but still there is a noticeable QQ component in the USD potential. Values of the overlap $x(\mathrm{QQ}|\mathrm{SU(3)})$ are ~ 0.4 for both configurations; this shows the persistence of the SU(3) algebraic structure with the QQ Hamiltonian despite the symmetry breaking spin-orbit interaction. The presence of the SU(3) component is still strong, in the USD potential for $N = 4$ nucleons with $x(\mathrm{SU(3)}|\mathrm{USD}) \sim 0.5$. For $N = 8$ and the USD potential, the overlap $x(\mathrm{SU(3)}|\mathrm{USD})$ is noticeably smaller than $x(\mathrm{QQ}|\mathrm{SU(3)})$, despite the similar values of the fractional collectivity b and of the quadrupole moment q shown in Fig. 5.3. Let us note parenthetically that there is a symmetry between indices λ and μ, which corresponds to particle-hole symmetry. Two configurations in Tab. 5.3 are particle-hole "mirrors" of each other, and their SU(3) representations are symmetric under exchange of λ and μ. The $(1s_{1/2}, 0d_{5/2}, 0d_{3/2})^6$ is not included in the table. It is a

half-filled shell, so its ground state is a degenerate mixture of the (6,0) and (0,6) representations.

Overall, the QQ Hamiltonian reproduces rotational modes for a range of models from a single-j to realistic shell model spaces, and its component is strong in the TBRE as well as in realistic potentials.

Table 5.1: Collective characteristics in the QQ Hamiltonian. Listed in the table are the values of the fractional collectivity b, quadrupole moments $q(2_1)$ and $q(2_2)$, and ratios of the transition rates b_{42} and the excitation energies R_{42}. The models are: N nucleons in a single $j = 19/2$ orbital and in two-level spaces $(13/2^+, 13/2^+)$ and $(13/2^+, 13/2^-)$ and N protons and neutrons in the $(0f_{7/2}, 1p_{3/2})$ and $(0f_{5/2}, 0g_{9/2})$ spaces with a splitting of the single-particle levels is $\delta\epsilon = \epsilon_{p_{3/2}} - \epsilon_{f_{7/2}}$ or $\delta\epsilon = \epsilon_{g_{9/2}} - \epsilon_{f_{5/2}}$. The energy scale in this case is given by the variance of the level spectrum for the two-particle system.

	$\delta\epsilon$	N	b	$q(2_1)$	$q(2_2)$	B_{42}	R_{42}
$(19/2)$		4	0.99	-0.98	0.84	1.41	3.29
		6	0.97	-0.98	0.87	1.42	3.31
		8	0.95	-0.97	0.85	1.43	3.27
$(13/2^+, 13/2^+)$		6	0.98	-0.98	-0.98	1.41	3.29
$(13/2^+, 13/2^-)$		6	0.98	-0.98	-0.98	1.41	3.29
$(0f_{7/2}, 1p_{3/2})$	0	8	0.97	0.99	-0.59	1.36	3.28
	0	10	0.89	0.98	-0.96	0.96	3.18
	0	12	0.99	0	0	1.32	3.07
$(0f_{7/2}, 1p_{3/2})$	0.6	8	0.97	0.99	-0.57	1.34	3.28
	0.6	10	0.90	0.97	-0.96	1.14	3.23
	0.6	12	0.97	0.28	-0.28	1.33	3.08
$(0f_{7/2}, 1p_{3/2})$	4.2	8	0.96	0.98	-0.39	1.36	3.30
	4.2	10	0.91	0.96	-0.95	1.36	3.29
	4.2	12	0.86	0.85	-0.85	1.44	3.24
$(0f_{7/2}, 1p_{3/2})$	-0.6	8	0.97	1.00	-0.60	1.35	3.26
	-0.6	10	0.88	0.97	-0.96	0.77	3.12
	-0.6	12	0.97	-0.28	0.28	1.33	3.08
$(0f_{5/2}, 0g_{9/2})$	0.6	8	0.97	-0.97	0.88	1.40	3.26

Table 5.2: Triaxiality characteristics in the QQ Hamiltonian. Listed in the table are the sums of excitation energy ratios $A \equiv R_{2_1 3_1} + R_{2_2 3_1}$ and $B \equiv 4R_{2_1 5_1} + R_{2_2 5_1}$ and three triaxiality parameters γ, Γ, and γ_{DF} (see Eqs. 4.1, 4.2, and 4.3). The models are the same as in our study of collectivity in random ensembles in Ch. 4 The two two-level models are degenerate, $\delta\epsilon = 0$, and non-degenerate with the single-particle energy splitting $\delta\epsilon = 4.2, 7$.

	N	$\delta\epsilon$	A	B	γ	Γ	γ_{DF}
$(19/2)$	6	-	1.005	1.026	9.79	0.43	7.52
$(19/2)$	8	-	0.986	1.002	12.59	0.52	7.41
$(0f_{7/2}, 1p_{3/2})$	8	0	1.051	1.227	4.68	-0.03	13.1
$(0f_{7/2}, 1p_{3/2})$	8	4.2	1.031	1.460	3.34	1.83	11.77
$(0f_{7/2}, 1p_{3/2})$	8	7	1.375	1.666	4.42	1.88	10.97

Table 5.3: Overlaps defined in (5.1) for N neutrons in the *sd* shell. Additionally to the values of the overlaps, the corresponding nucleus and the ground state SU(3) representation are listed for each valence configuration. The values of the single-particle energies for the QQ model are chosen according to the spin-orbit splitting: $\epsilon(d_{5/2}) = -kl/2$ and $\epsilon(d_{3/2}) = k(l+1)/2$ with $k = 2.0$ (light blue line in Fig. 5.3).

N	Nucleus	(λ, μ)	x(QQ|USD)	x(QQ|SU(3))	x(SU(3)|USD)
4	^{20}O	(4,2)	0.878	0.605	0.454
8	^{24}O	(2,4)	0.425	0.595	0.103

CHAPTER 6

CONCLUSION

In this thesis the quadrupole collectivity that emerges in systems with random two-body interactions is examined. A low-lying spectrum, characteristic of a rigid rotor, is commonly observed. The transition $B(E2, 0_{gs} \rightarrow 2_1)$, the quadrupole moment of the 2_1 state, and the deexcitation ratio $B(E2, 4_1 \rightarrow 2_1)/B(E2, 2_1 \rightarrow 0_{gs})$ are all consistent with that of a deformed rotor.

A weak triaxiality is further determined. For this purpose the method of identifying triaxiality based on the signatures of the low-lying spectrum is proposed. It allows one to deduce the degree of triaxiality γ and the degree of asymmetry of the triaxial Hamiltonian Γ independently. This method also provides a comparison of the quadrupole triaxiality with the triaxiality from the Hamiltonian, with a given assumption for moments of inertia.

The quadrupole behavior in random ensembles appears to emerge due to the quadrupole-quadrupole interaction component in the Hamiltonian. This component, as well as some higher multipoles can establish a noticeable coherence despite the overall many-body randomness and complexity. Similarly to the moment-of-inertia-like J^2 term (that is responsible for the ground state configurations with the maximum possible spin) the QQ (quadrupole-quadrupole) component, while not a constant of motion, is dynamically prevailing. This is supported by the following arguments: (i) The fraction of random realizations that are quadrupole-collective is extremely

large as compared to the statistically expected number. (ii) In the two-body random ensemble, the quadrupole collectivity displayed by the transition rates disappears when the QQ component in the interaction is removed. (iii) Collective states in the TBRE have structure similar to that of the QQ Hamiltonian eigenstates. (iv) The type of the quadrupole deformation and most of the quantitative measures in the TBRE are consistent with those of the QQ Hamiltonian.

In light of this finding the characteristics of the QQ Hamiltonian, for which the geometry of the configuration space is the only parameter, are investigated. Deformed mean field and rotational behaviour are induced by the QQ Hamiltonian in all studied cases. It appears that the single-particle level structure, which represents the mean-field structure of the core, affects the shape of deformation. Due to particle-hole symmetry, which does not need to be exact, the number of prolate and oblate configurations is approximately the same within a given valence space, although in some cases the single-particle splitting leads to the asymmetry in the number of prolate and oblate shapes. The role of the single-particle level structure in the prolate predominance discussed by Hamamoto in Ref. [44], our results for the QQ interaction appear to be consistent with the effect discussed in this reference. The QQ interaction is also an important component of realistic potential: we showed that its structure to a great extent survives in the USD potential for rotational nuclei in the *sd*-shell.

APPENDIX A

$E2$ TRANSITION RATES IN THE SENIORITY SCHEME ON ONE LEVEL

In order to find matrix elements of the quadrupole operator $\langle J_f M_f|\mathcal{M}^\dagger_{2k}|J_i M_i\rangle$, and thus the $B(E2, J_i \to J_f)$ transition in the N-particle configuration, we first find its matrix elements $\langle L_f\Lambda_f|\mathcal{M}_{2k}|L_i\Lambda_i\rangle$ in the two-body configuration. The pair-creation operator $P^{(\alpha)\dagger}_{L\Lambda}$ in the Hamiltonian (1.2) can be written in terms of the Wigner 3-j symbols

$$P^{(\alpha)\dagger}_{L\Lambda} = \frac{(-)^{L-M}}{\sqrt{2}} \sum_{m_1 m_2} (2L+1) \begin{pmatrix} j & L & j \\ m_1 & -\Lambda & m_2 \end{pmatrix} a^\dagger_{m_1} a_{m_2}. \tag{A.1}$$

The quadrupole operator in the second quantization takes on a form

$$\mathcal{M}_{2k} = \sum_{\lambda\mu} (-1)^{j-\lambda} \begin{pmatrix} j & 2 & j \\ -\lambda & k & \mu \end{pmatrix} a^\dagger_\mu a_\lambda, \tag{A.2}$$

with $e_{\text{eff}}\langle j|r^2|j\rangle$ taken to be a unit. Then the quadrupole matrix elements become

$$\langle L_f\Lambda_f|\mathcal{M}^\dagger_{2k}|L_i\Lambda_i\rangle = 2(-1)^{\Lambda_i}\sqrt{(2L_i+1)(2L_f+1)} \begin{pmatrix} L_f & L_i & 2 \\ -\Lambda_f & \Lambda_i & k \end{pmatrix} \begin{Bmatrix} L_f & L_i & 2 \\ j & j & j \end{Bmatrix}, \tag{A.3}$$

here we used a property that of a product of three 3-j symbols can be written as a product of 3-j and 6-j symbols.

The quadrupole moment is a vector in the quasi-spin space [1], and thus we can use the Wigner-Eckart theorem. An N-body state $|SS^{(N)}_z\rangle$ is defined by the quasi momentum $S = (\Omega/2 - \nu)/2$ and its projection $S^{(N)}_z = (N - \Omega/2)/2$, and thus

the reduced matrix element is the same between N-particle states with qausi-spin projection $S_z^{(N)}$ and between two-particle states with qausi-spin projection $S_z^{(2)}$. For two particular states of interest 2_1 and 4_1, which are of the same seniority $\nu = 2$,the quasi-spin is the same, S, and the Wigner-Eckart theorem yields to

$$\begin{aligned}\langle SS_z^{(N)}|\mathcal{M}_{2k}^{\dagger}|SS_z^{(N)}\rangle &= (-1)^{S-S_z^{(N)}} \begin{pmatrix} S & 1 & S \\ -S_z^{(N)} & 0 & S_z^{(N)} \end{pmatrix} \langle S||\mathcal{M}_2^{\dagger}||S\rangle \\ &= 2S_z^{(N)}/\sqrt{(2S+2)(2S+1)(2S)}\langle S||\mathcal{M}_2^{\dagger}||S\rangle \end{aligned} \tag{A.4}$$

and

$$\langle SS_z^{(2)}|\mathcal{M}_{2k}^{\dagger}|SS_z^{(2)}\rangle = 2S_z^{(2)}/\sqrt{(2S+2)(2S+1)(2S)}\langle S||\mathcal{M}_2^{\dagger}||S\rangle, \tag{A.5}$$

thus

$$\langle SS_z^{(N)}|\mathcal{M}_{2k}^{\dagger}|SS_z^{(N)}\rangle = \frac{(2N-\Omega)}{(4-\Omega)}\langle SS_z^{(2)}|\mathcal{M}_{2k}^{\dagger}|SS_z^{(2)}\rangle. \tag{A.6}$$

The matrix elements in the two-particle configurations were found in Eq. (A.3). Thus, the the matrix elements in the N-body configuration are

$$\begin{aligned}\langle J_f M_f|\mathcal{M}_{2k}^{\dagger}|J_i M_i\rangle &= (-1)^{M_i}\frac{2(2N-\Omega)}{(4-\Omega)}\sqrt{(2M_i+1)(2M_f+1)} \\ &\times \begin{pmatrix} J_f & J_i & 2 \\ -M_f & M_i & k \end{pmatrix} \begin{Bmatrix} J_f & J_i & 2 \\ j & j & j \end{Bmatrix}, \end{aligned} \tag{A.7}$$

with the reduced matrix elements:

$$\langle J_f||\mathcal{M}_2^{\dagger}||J_i\rangle = (-1)^{J_i+M_i-M_f}\frac{2(2N-\Omega)}{(4-\Omega)}\sqrt{(2J_f+1)(2J_i+1)} \begin{Bmatrix} J_f & J_i & 2 \\ j & j & j \end{Bmatrix}. \tag{A.8}$$

The definition of the reduced transition probability (3.2) can be rewritten as

$$B(E\lambda, J_i \to J_f) = \frac{|\langle J_f||\mathcal{M}_\lambda||J_i\rangle|^2}{2J_i+1}, \tag{A.9}$$

and the reduced transition probability between any two states of the same seniority is

$$B(E\lambda, J_i \to J_f) = 4\left(\frac{(2N-\Omega)}{(4-\Omega)}\right)^2 (2J_f+1) \begin{Bmatrix} J_f & J_i & 2 \\ j & j & j \end{Bmatrix}^2. \tag{A.10}$$

APPENDIX B

SU(3) IRREDUCIBLE REPRESENTATIONS FOR THE GROUND STATE BAND

In this appendix we show how to determine a ground state SU(3) mulitplet on example of the pf shell. The pf shell ($n = 3$) is ten-fold degenerate and thus there are ten combinations $(n_x n_y n_z)$, where n_i is a number of quanta in the corresponding direction. These combinations $(n_x n_y n_z)$ are representations of the U(3) group and listed below in the order proposed in Ref. [27]:

$$
\begin{array}{cccccc}
\text{Holes} & \rightarrow & & & & \\
\text{Particles} & (0\ 0\ 3) \rightarrow & (1\ 0\ 2) \rightarrow & (2\ 0\ 1) \rightarrow & (3\ 0\ 0) \\
\Downarrow & & \Downarrow & \Downarrow & \Downarrow \\
 & & (0\ 1\ 2) \rightarrow & (1\ 1\ 1) \rightarrow & (2\ 1\ 0) \\
 & & & \Downarrow & \Downarrow \\
 & & & (0\ 2\ 1) \rightarrow & (1\ 2\ 0) \\
 & & & & \Downarrow \\
 & & & & (0\ 3\ 0)
\end{array}
$$

The two SU(3) quantum numbers are: $\lambda = n_z - n_x$ and $\mu = n_x - n_y$. In order for the energy $E = -4([\lambda^2 + \mu^2 + \lambda\mu + 3(\lambda + \mu)]$ to be the lowest, particles should be distributed along the rows of the table for less than half filled shells, this is marked with an arrow. For more than half filled shells (holes), particles should be distributed along the columns of the table. This result is not trivial, one can see Ref. [27] for a detailed proof.

Table B.1: The ground state representations of the U(3) group $(n_x n_y n_z)$ and of the SU(3) group (λ, μ) for N particles in the pf shell.

N	$(n_x n_y n_z)$	(λ, μ)
1	(0 0 3)	(3,0)
2	(0 0 3)+(1 0 2)=(1 0 5)	(4,1)
3	(1 0 5)+(0 1 2)=(1 1 7)	(6,0)
4	(1 1 7)+(2 0 1)=(3 1 8)	(5,2)
5	(3 1 8)+(1 1 1)=(4 2 9)	(5,2)
6	(0 0 3)+(1 0 2)+(2 0 1)+(3 0 0)+(0 1 2)+(1 1 1) =(7 2 9)	(2,5)
7	(7 2 9)+(2 1 0)=(9 3 9)	(0,6)
8	(9 3 9)+(0 2 1)=(9 5 10)	(1,4)
9	(9 5 10)+(1 2 0)=(10 7 10)	(0,3)

The summation of the $(n_x n_y n_z)$ representations is illustrated in the table below for $N = 1..9$ particles. Given there are also SU(3) irreps (λ, μ) for the ground state.

In order to generate all SU(3) multiplets in a given configurations, one has to repeat the same procedure as for the ground state, but for all possible distributions of particles. This can give redundant (equivalent) representations which should be excluded.

BIBLIOGRAPHY

[1] P. Schuck P. Ring. *The nuclear many-body problem*. New York: Springer-Verlag, 1980.

[2] A. Bohr and B. R. Mottelson. *Nuclear structure*, volume 2. W. A. Benjamin, New York, 1974.

[3] V. Zelevinsky and A. Volya. Nuclear structure, random interactions and mesoscopic physics. *Phys. Rep.*, 391(3-6):311, 2004.

[4] C. W. Johnson and H. A. Nam. New puzzle for many-body systems with random two-body interactions. *Phys. Rev. C*, 75(4):047305, 2007.

[5] T. Papenbrock and H. A. Weidenmuller. Colloquium: Random matrices and chaos in nuclear spectra. *Rev. Mod. Phys.*, 79(3):997, 2007.

[6] Y. M. Zhao, A. Arima, and N. Yoshinaga. Regularities of many-body systems interacting by a two-body random ensemble. *Phys. Rep.*, 400(1):1, 2004.

[7] J. P. Elliott. Collective motion in the nuclear shell model. ii. the introduction of intrinsic wave-functions. *Proc. Roy. Soc.*, 245(1243):562, 1958.

[8] E.P. Wigner. On the distribution of the roots of certain symmetric matrices. *Ann. Math*, 67:325, 1958.

[9] N. Bohr. Neutron capture and nuclear constitution. *Nature*, 137:344, 1936.

[10] M.L. Mehta. *Random Matrices*. Elsevier/Academic Press, San Diego, 2004.

[11] K. K. Mon and J. B. French. Statistical properties of many-particle spectra. *Ann. Phys. (N.Y.)*, 95(90):90, 1975.

[12] J.B. French and S.S.M. Wong. Validity of random matrix theories for many-particle systems. *Phys. Lett. B*, 33(7):449, 1970.

[13] O. Bohigas and J. Flores. Two-body random hamiltonian and level density. *Physics Letters B*, 34(4):261 – 263, 1971.

[14] V. Zelevinsky, B. A. Brown, N. Frazier, and M. Horoi. The nuclear shell model as a testing ground for many-body quantum chaos. *Physics Reports*, 276(2-3):85 – 176, 1996.

[15] C. W. Johnson, G. F. Bertsch, and D. J. Dean. Orderly spectra from random interactions. *Phys. Rev. Lett.*, 80:2749, 1998.

[16] H. A. Weidenmüller and G. E. Mitchell. Random matrices and chaos in nuclear physics: Nuclear structure. *Reviews of Modern Physics*, 81(2):539, 2009.

[17] D. Mulhall, A. Volya, and V. Zelevinsky. Geometric chaoticity leads to ordered spectra for randomly interacting fermions. *Phys. Rev. Lett.*, 85(19):4016–4019, 2000.

[18] R. Bijker, A. Frank, and S. Pittel. Dominance of $J^p = 0^+$ ground states in even-even nuclei from random two-body interactions. *Phys. Rev. C*, 60(2):021302, 1999.

[19] `http://cosmo.volya.net`.

[20] Y. M. Zhao, A. Arima, N. Shimizu, K. Ogawa, N. Yoshinaga, and O. Scholten. Patterns of the ground states in the presence of random interactions: Nucleon systems. *Phys. Rev. C*, 70(5):054322, 2004.

[21] L. D. Landau and L. M. Lifshitz. *Quantum Mechanics Non-Relativistic Theory.* London, Pergamon Press; Reading, Mass., Addison-Wesley Pub. Co., 1958.

[22] A. S. Davydov and G. F. Filippov. Rotational states in even atomic nuclei. *Nucl. Phys.*, 8:237, 1958.

[23] J. L. Wood, A-M. Oros-Peusquens, R. Zaballa, J. M. Allmond, and W. D. Kulp. Triaxial rotor model for nuclei with independent inertia and electric quadrupole tensors. *Phys. Rev. C*, 70(2):024308, 2004.

[24] J. M. Allmond. *Studies of triaxial rotors and band mixing in nuclei.* PhD thesis, Georgia Institute of Technology, 2007.

[25] Malcolm Harvey. *The Nuclear SU3 Model*, volume 1 of *Advances in Nuclear Physics*, page 67. Plenum Press, New York, 1968.

[26] D. J. Rowe. Dynamical symmetries of nuclear collective models. *Prog.Part. Nucl. Phys.*, 37:265, 1996.

[27] S. T. Belyaev, I. M. Pavlichenkov, and Yu F. Smirnov. A study of the generalized density matrix in the su(3) model of elliott for an arbitrary oscillator n-shell. *Nuclear Physics A*, 441(1):33, 1985.

[28] G. Thiamova, D. J. Rowe, and J. L. Wood. Coupled-SU(3) models of rotational states in nuclei. *Nuclear Physics A*, 780(3-4):112, 2006.

[29] G. Racah. Theory of complex spectra. ii. *Phys. Rev.*, 62:438, 1942.

[30] G. Racah. Theory of complex spectra. iii. *Phys. Rev.*, 63:367, 1943.

[31] A. Shalit and I. Talmi. *Nuclear shell theory.* New York: Academic Press, 1963.

[32] I. Talmi. Energies of $f_7/2^n$ nuclear configurations. *Phys. Rev.*, 107(1):326–327, 1957.

[33] A. Volya, B. A. Brown, and V. Zelevinsky. Exact solution of the nuclear pairing problem. *Phys. Lett. B*, 509(1-2):37, 2001.

[34] P. Chau Huu-Tai, A. Frank, N. A. Smirnova, and P. Van Isacker. Geometry of random interactions. *Phys. Rev. C*, 66(6):061302, 2002.

[35] A. Volya. Interplay of pairing and multipole interactions in a simple model. *Phys. Rev. C*, 65(4):044311, 2002.

[36] R. Casten. *Nuclear structure from a simple perspective*, volume 23. Oxford University Press, 2000.

[37] J. M. Allmond, R. Zaballa, A. M. Oros-Peusquens, W. D. Kulp, and J. L. Wood. Triaxial rotor model description of e2 properties in^{186,188,190,192}os. *Phys. Rev. C*, 78(1):014302, 2008.

[38] V. Zelevinsky, D. Mulhall, and A. Volya. Do we understand the role of incoherent interactions in many-body physics? *Phys. Atom. Nucl.*, 64:525–535, 2001.

[39] V. Zelevinsky, A. Volya, and N. Auerbach. Nuclear schiff moment and soft vibrational modes. *Phys. Rev. C*, 78(1):014310, 2008.

[40] M. Horoi and V. Zelevinsky. Random interactions explore the nuclear landscape: Predominance of prolate nuclear deformations. *Phys. Rev. C*, 81(3):034306, 2010.

[41] B. Castel and K. Goeke. Prolate-oblate energy difference and shape variation in the $f-p$ shell. *Phys. Rev. C*, 13(4):1765–1767, 1976.

[42] B. Castel, D. J. Rowe, and L. Zamick. Why are deformed nuclei prolate? *Physics Letters B*, 236(2):121, 1990.

[43] N. Tajima, Y. R. Shimizu, and N. Suzuki. Origin of prolate dominance of nuclear deformation. *Prog.Theor.Phys.Suppl.*, (146):628, 2002.

[44] I. Hamamoto and B. R. Mottelson. Further examination of prolate-shape dominance in nuclear deformation. *Phys. Rev. C*, 79(3):034317, 2009.

[45] W. A. Richter, M. G. Van Der Merwe, R. E. Julies, and B. A. Brown.

[46] B. H. Wildenthal. Empirical strengths of spin operators in nuclei. *Progress in Particle and Nuclear Physics*, 11:5 – 51, 1984.

BIOGRAPHICAL SKETCH

Volha Abramkina earned her bachelor's degree in physics from Grodno State University in 2000. In 2004 she began her graduate studies at Florida State University and later joined the Theoretical Nuclear Physics group. After earning a master's degree in 2006 she moved to the University of Illinois at Urbana-Champaign where, as a graduate student, she conducted research in biophysics. In 2007 she returned to Florida State University and resumed her work in theoretical nuclear physics under the direction of Dr. Alexander Volya. In summer 2011, she successfully defended her dissertation.